Consecutive (Pseudo-)Four-Component Synthesis of Meta- and Ortho-Biaryl Triarylamines with Tunable Emission and Redox Properties

Regina Kohlbecher, Tim Lippert, Hendrik Schröder, Dustin N. Jordan, Christoph Janiak, Thomas J. J. Müller

Suggested Citation:
Kohlbecher, R., Lippert, T., Schröder, H., Jordan, D. N., Janiak, C., & Müller, T. J. J. (2026). Consecutive (Pseudo-)Four-Component Synthesis of Meta- and Ortho-Biaryl Triarylamines with Tunable Emission and Redox Properties. European Journal of Organic Chemistry, 29(9), Article e70312. https://doi.org/10.1002/ejoc.70312

European Journal of Organic Chemistry

EurJOC
European Journal of Organic Chemistry

Chemistry Europe
European Chemical Societies Publishing

RESEARCH ARTICLE Very Important Paper

Consecutive (*Pseudo*-)Four-Component Synthesis of *Meta*- and *Ortho*-Biaryl Triarylamines with Tunable Emission and Redox Properties

Regina Kohlbecher[1] | Tim Lippert[1] | Hendrik Schröder[1] | Dustin N. Jordan[2] | Christoph Janiak[2] | Thomas J. J. Müller[1]

[1]Mathematisch-Naturwissenschaftliche Fakultät, Institut für Organische Chemie und Makromolekulare Chemie, Heinrich-Heine-Universität Düsseldorf, Düsseldorf, Germany | [2]Mathematisch-Naturwissenschaftliche Fakultät, Institut für Anorganische Chemie und Strukturchemie, Heinrich-Heine-Universität Düsseldorf, Düsseldorf, Germany

Correspondence: Thomas J. J. Müller (ThomasJJ.Mueller@hhu.de)

Received: 29 November 2025 | **Revised:** 11 December 2025 | **Accepted:** 17 December 2025

Keywords: biaryl twisting | cross-coupling | multicomponent syntheses | substituent effects | triarylamine

ABSTRACT

The strategic combination of Suzuki coupling and Buchwald–Hartwig amination in consecutive (*pseudo*-)four-component syntheses provides a highly efficient and modular route to *meta*- and *ortho*-biaryl-substituted triarylamines (*m*- and *o*-bTAA), thereby expanding a substance library that has previously focused on *para*-bTAA. The broad range of novel bTAA enables comprehensive investigations of their electronic properties and reveals highly tunable emission in solution from blue to yellow, with quantum yields up to 55%, and up to 26% in the solid state. The bTAA also show strong potential as stimulus-responsive luminophores due to their pronounced positive emission solvatochromism, which indicates substantial charge transfer character—particularly in the *m*-bTAA—as well as aggregation-induced emission in DMSO/water mixtures with with intensity enhancements of up to 75-fold. Quantitative 2D Hammett correlations combined with quantum-chemical calculations systematically rationalize substituent effects not only on the emission properties but also on the low, reversible redox potentials determined by cyclic voltammetry. Cyclic voltammetry further reveals irreversible dimerization processes in certain unsubstituted bTAA. In addition to *para*-substituents, the biaryl substitution pattern (*meta*, *ortho*, or *para*) also proves to be a finely tunable parameters, opening new opportunities for the rational design of tailored bTAA emitters with predictable structure–property relationships.

1 | Introduction

The investigation of structure–property relationships (SPR) has long provided a foundation for the rational design of chemical reactivity and tailored material properties [1, 2], with linear free-energy relationships such as the Hammett equation serving as key tools [3–5]. By quantifying substituent effects, these relationships enable predictive analysis of the interplay between thermodynamic and kinetic parameters and are therefore indispensable across materials science and organic electronics [6–10]. One prominent example of a SPR is aggregation-induced emission (AIE), originally reported by B. Z. Tang and coworkers in 2001 [11–15]. In contrast to conventional fluorophores whose emission is generally quenched upon aggregation [16], AIE-active dyes displaying weak or negligible emission in solution yet exhibit pronounced luminescence in the aggregated state [11, 17]. In triarylamines (TAA), this behavior arises from the restricted rotational freedom of their propeller-like structure, whereby aggregation hampers nonradiative decay pathways and favors radiative ones [16]. The AIE characteristics of TAA render them excellent candidates for applications ranging from cell imaging and photodynamic cancer therapy to serving as emitter layers in organic light-emitting diodes (OLED) [18, 19].

Dedicated to Irmtraud Kohlbecher on the occasion of her 90th birthday.

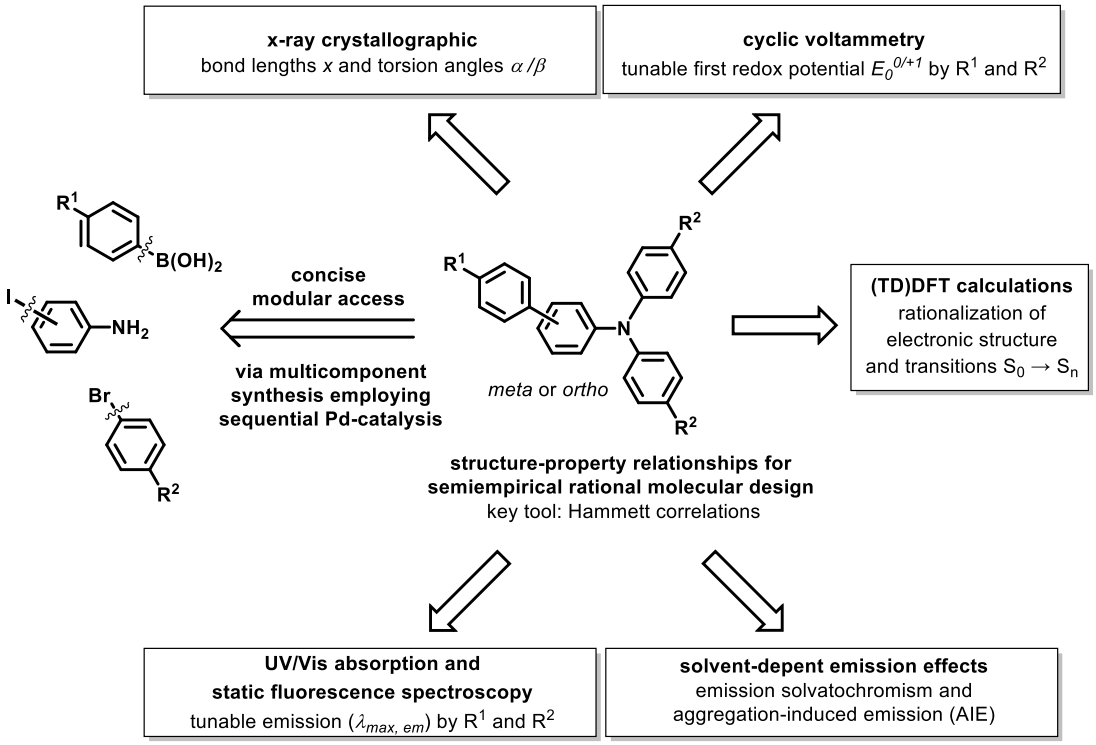

FIGURE 1 | Schematic summary of the synthetic, electrochemical, photophysical, and electronic-structure aspects outlined in this work.

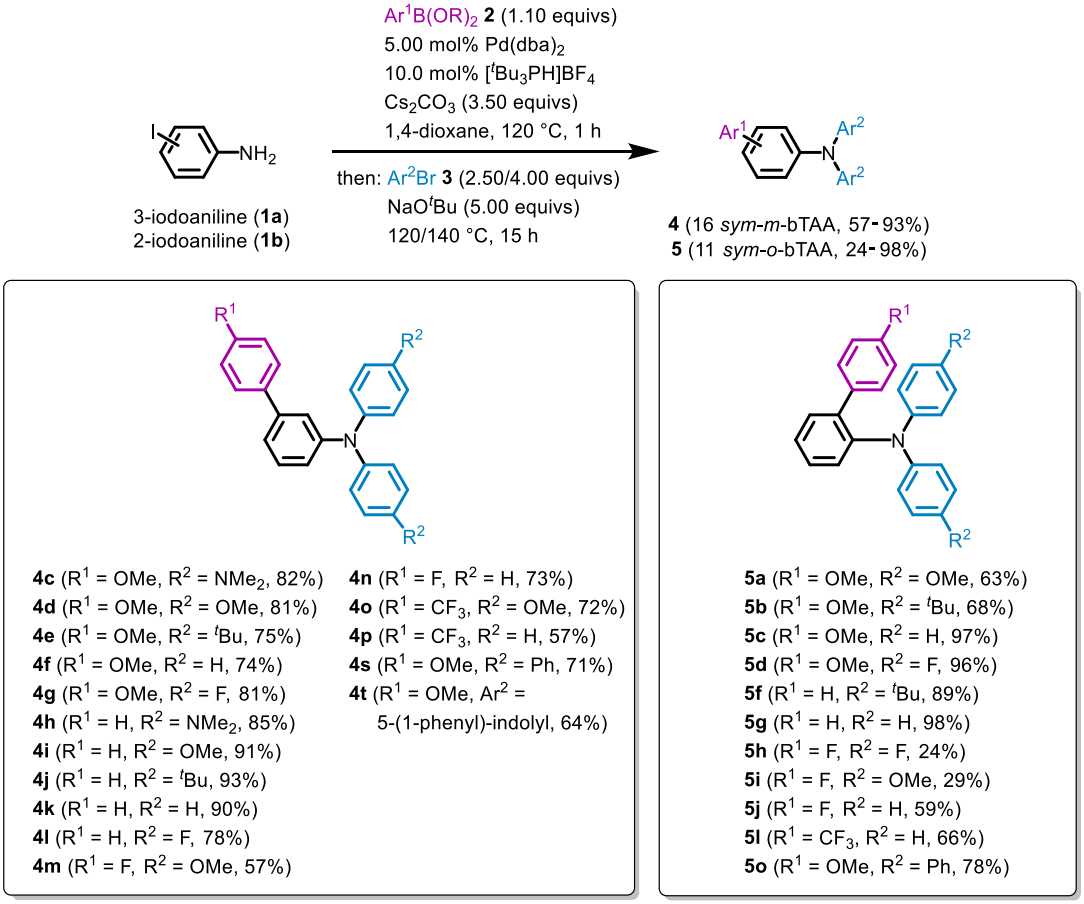

SCHEME 1 | *Pseudo*-four-component synthesis of *sym-m*-bTAA **4** and *sym-o*-bTAA **5** ($B(OR)_2$ = $B(OH)_2$, Bpin).

Introducing bulky biaryl groups enhances solubility as well as processability [20]. Biaryl-substituted TAA (bTAA) exhibit outstanding crystallizability, enabling applications in sensing, bioimaging, and anticounterfeiting technologies [21]. In addition, TAA possess low reversible redox potentials and readily form stable radical cations, underpinning their established role as hole-transport materials in OLED [20]. Oxidation of the simplest TAA, triphenylamine (TPA), also provides access to dimers, i.e., *N*,*N*′-tetraaryl benzidines [22, 23]. These benzidines constitute a key class of organic compounds which, due to their low oxidation potentials, have been established as outstanding hole-transport materials in OLED [24], organic solar cells [20], perovskite solar cells [25], and diverse sensing applications [26, 27].

Developing a detailed SPR framework for the rational molecular design of bTAA for specific applications requires an efficient tool

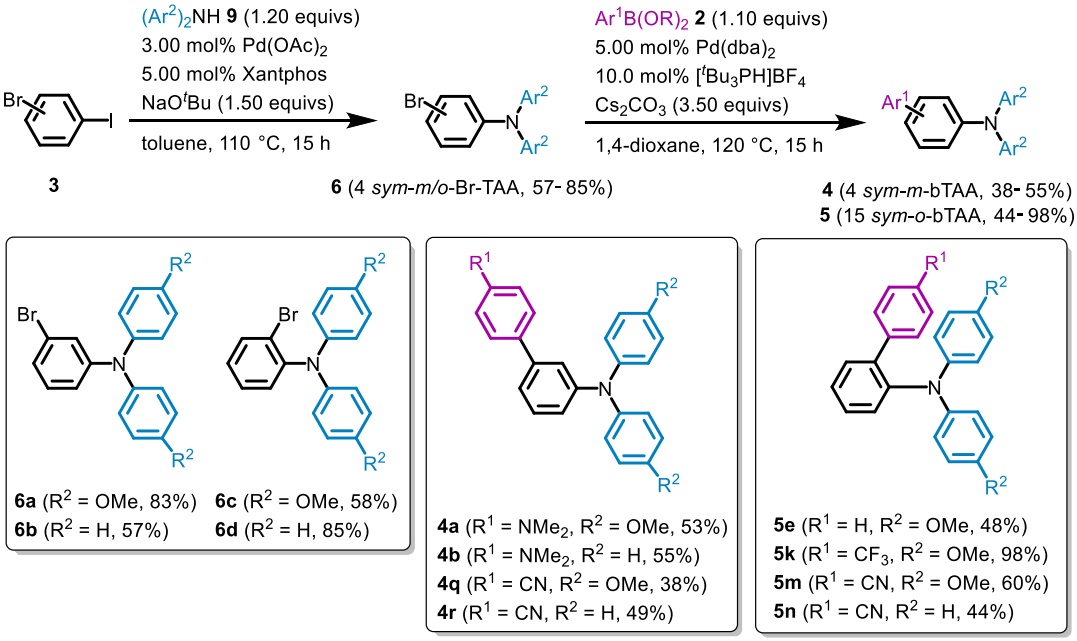

SCHEME 2 | Two-step synthesis of *sym-m*-bTAA **4a-b** and **4q-r** as well as the *sym-o*-bTAA **5e**, **5k,** and **5m-n** with separate Suzuki coupling and Buchwald–Hartwig amination ($B(OR)_2$ = $B(OH)_2$, Bpin).

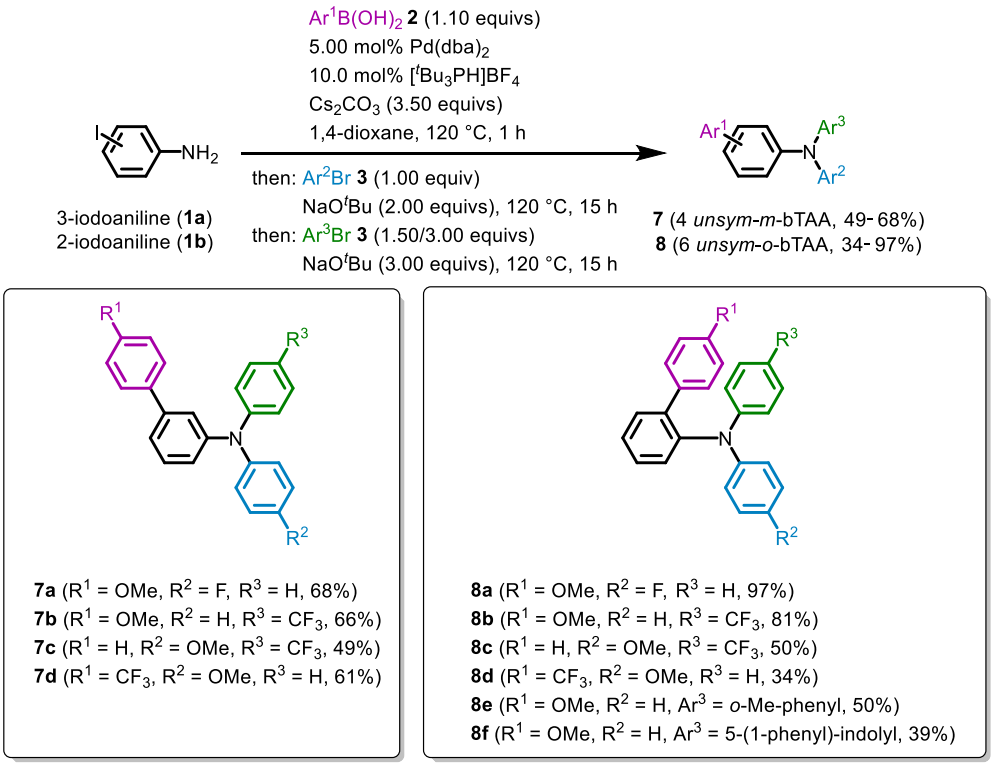

SCHEME 3 | Four-component synthesis of *unsym-m*-bTAA **7** and *unsym-o*-bTAA **8**.

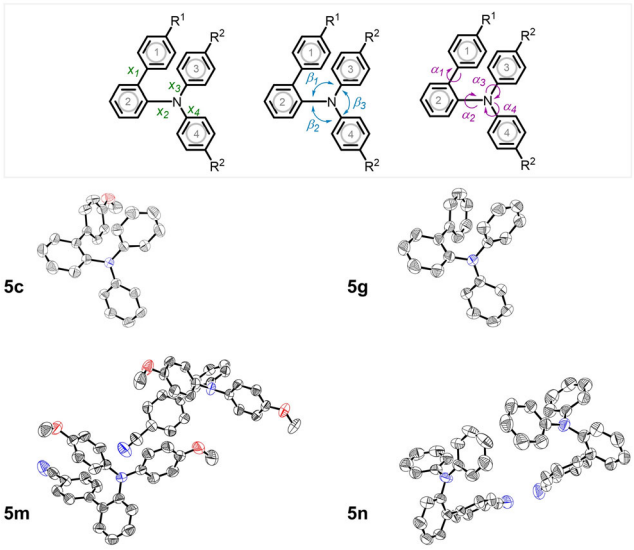

FIGURE 2 | Illustration of the different bond lengths x and angles β/α (above) and visualization of the molecular structures of selected *sym-o*-bTAA **5** derivatives in their respective crystal structure (below, the thermal ellipsoids (50% probability), with all hydrogen atoms hidden for clarity).

for rapidly providing suitable structures. Multicomponent reactions (MCRs) represent a modern synthetic concept that enables rapid and diversity-oriented access to compound libraries [28, 29]. By definition, MCRs enable the generation of target structures from three or more reactants within a single reaction vessel. As one-pot processes, they incorporate a substantial proportion of the starting atoms into the final product, while greatly minimizing the effort associated with isolation [30]. With the growing focus on sustainability, efficient one-pot processes are gaining importance, the combination of MCRs and sequential Pd catalysis stands out as a particularly resource-saving strategy [31, 32]. Sequential Pd-catalyzed synthetic methods have increasingly proven to be powerful tools that enable the construction of complex molecular architectures with high efficiency, selectivity, and atom economy [33]. In particular, cross-couplings are useful due to a broad tolerance toward functional groups [34–36].

Recently, we have developed a successful merger of Suzuki coupling and Buchwald–Hartwig amination within a consecutive MCR for efficiently accessing functionalized phenothiazines, carbazoles, indoles, and *para*-bTAA (*p*-bTAA) [37–39]. Here, we report on an advancement of the highly diversified sequential

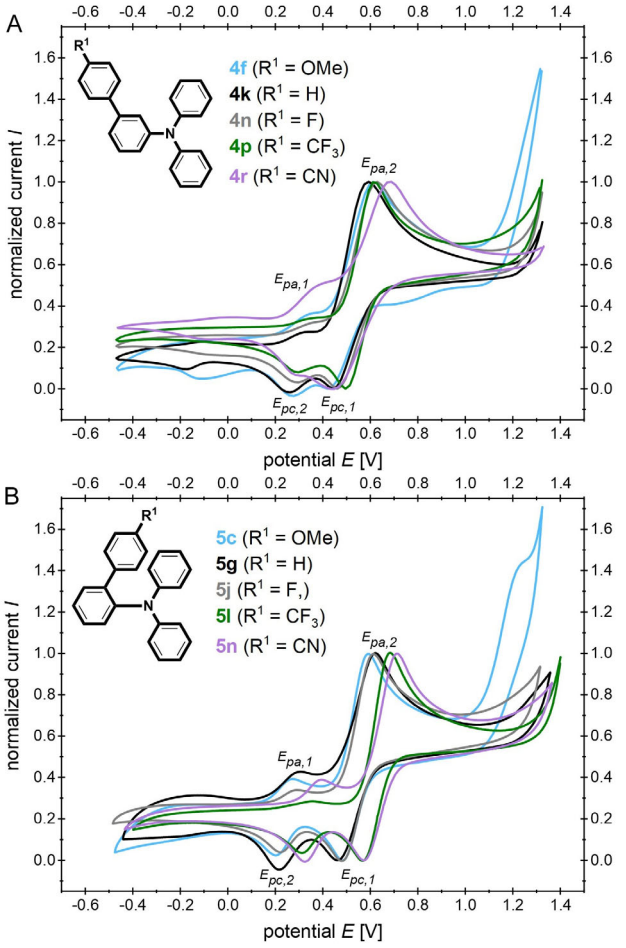

FIGURE 3 | Cyclic voltammograms of (**A**) *sym-m*-bTAA **4f**, **4k**, **4n**, **4p**, and **4r** and (**B**) *sym-o*-bTAA **5c**, **5g**, **5j**, **5l**, and **5n** with a variously substituted biaryl moiety R^1 in comparison ($R^2 = H$, recorded in CH_2Cl_2, $T = 293$ K, $v = 100$ mV/s, electrolyte: [^{n}Bu$_4$N][PF$_6$], Pt working electrode, Pt counter electrode, Ag/AgCl reference electrode, redox standard: decamethylferrocene $E_0^{0/+1} = -0.54$ V (vs. ferrocene $E_0^{0/+1} = 0.00$ mV [45])).

Pd-catalyzed consecutive MCR, which gives rise to the concise and selective synthesis of *meta*- (*m*-) and *ortho*- (*o*-) bTAA from simple starting materials (Figure 1). In addition, systematic correlation analysis of electrochemical and photophysical properties, complemented by quantum-chemical calculations, the SPR of *m*- and *o*-bTAA in comparison with *p*-bTAA provides deeper insight into their electronic structure [39].

TABLE 1 | Bond lengths and angles from the crystal structures of selected *sym-o*-bTAA **5**.

Compounds	R^1	R^2	Bond lengths x, Å			Bond angles β, °				Torsion angle α, °			
			x_1	x_2	x_3	x_4	β_1	β_2	β_3	α_1	α_2	α_3	α_4
5c	OMe	H	1.483	1.436	1.416	1.417	118	118	122	53	67	40	16
5g	H	H	1.486	1.433	1.423	1.411	120	117	123	56	59	33	34
5n	CN	H	1.482	1.436	1.429	1.406	116	122	121	56	72	25	41
			1.484	1.431	1.432	1.407	116	120	122	62	74	29	42
5m	CN	OMe	1.483	1.427	1.432	1.414	120	116	119	49	60	49	39
			1.488	1.421	1.427	1.427	119	118	119	57	59	62	27

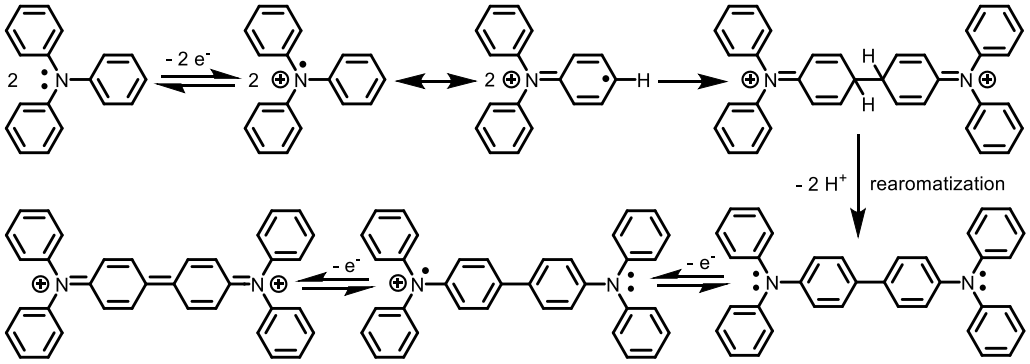

SCHEME 4 | Dimerization mechanism on the example of TPA after electrochemical oxidation.

TABLE 2 | Selected electrochemical properties (first redox potential $E_0^{0/+1}$ of monomer, first and second redox potential $E_{0,\text{dimer}}^{0/+1}$ and $E_{0,\text{dimer}}^{+1/+2}$ of the dimer formed in situ) of (*un*)*sym*-*m*-bTAA **4/7** or (*un*)*sym*-*o*-bTAA **5/8** with dimerization processes.

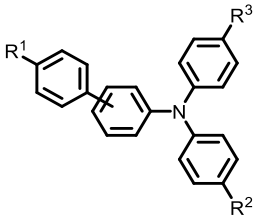

Compound	R^1	R^2	R^3	$E_0^{0/+1}$, V[a]	$E_{0,\text{dimer}}^{0/+1}$, V[a]	$E_{0,\text{dimer}}^{+1/+2}$, V[a]
4f	OMe	H	H	0.54	0.31	0.54
4g	OMe	F	F	0.60	0.42	0.60
4k	H	H	H	0.51	0.30	0.51
4l	H	F	F	0.54	0.41	0.54
4n	F	H	H	0.54	0.31	0.54
4p	CF_3	H	H	0.54	0.31	0.54
4q	CN	OMe	OMe	0.31	0.12	0.31
4r	CN	H	H	0.56	0.31	0.56
5c	OMe	H	H	0.54	0.26	0.54
5g	H	H	H	0.52	0.26	0.52
5j	F	H	H	0.54	0.24	0.54
5l	CF_3	H	H	0.60	0.32	0.60
5n	CN	H	H	0.63	0.35	0.63
5a	OMe	F	H	0.76	0.30	0.76
7a	OMe	F	H	0.58	0.38	0.58
7b	OMe	H	CF_3	0.64	−0.07	0.64
7d	CF_3	OMe	H	0.51	0.21	0.51
8b	OMe	H	CF_3	0.71	0.51	0.71
8e	OMe	*o*-Me	H	0.57	0.26	0.57
8f	OMe	Indolyl	H	0.58	−0.04	0.58

[a]Recorded in CH_2Cl_2, $T = 293$ K, extrapolation of data with $v = 100$, 250, 500, and 1000 mV/s to 0.00 mV/s, electrolyte: [^{n}Bu$_4$N][PF$_6$], Pt working electrode, Pt counter electrode, Ag/AgCl reference electrode, $E_0 = \frac{(E_{pa} - E_{pc})}{2}$ with redox standard: decamethylferrocene $E_0^{0/+1} = -0.54$ V (vs. ferrocene $E_0^{0/+1} = 0.00$ mV [45]).

2 | Results and Discussion

2.1 | Syntheses

The successful approach to symmetrically (*sym*) *N*,*N*-substituted *p*-bTAA (*sym*-*p*-bTAA) [39] prompted us to gain deeper insight into the positional effects of the biaryl unit of *sym*-*m*-bTAA and *sym*-*o*-bTAA on selectivity, reactivity, and the broad range of electrochemical and photophysical properties. Based on this concept and starting from 3-iodoaniline (**1a**) and arylboronic acid(ester)s **2** followed by addition of aryl bromides **3**, the optimized *pseudo*-four-

component synthesis after flash chromatography gives rise to the formation of a diverse library of 16 *sym-m*-bTAA **4** derivatives in yields between 57 and 93% (Scheme 1). By choosing a mono-iodinated substrate **1** for the first step (Suzuki coupling) before the second step (Buchwald–Hartwig amination), a homocoupling can be avoided. As reported previously [31, 37–39], the same catalyst system, i.e., $Pd(dba)_2$-[$^tBu_3PH$]BF_4, is effective in both catalytic steps that are now concatenated in the sense of a Suzuki–Buchwald–Hartwig (SBH) sequence in a one-pot fashion. A crucial factor is the choice of the appropriate bases for the individual coupling steps in the sequence. While Suzuki coupling can be carried out with the weaker base cesium carbonate, Buchwald–Hartwig amination requires the stronger base NaO^{t}Bu [39]. Strictly anhydrous conditions are essential, as even trace amounts of water will convert the base into inactive hydroxides for the amination step and thereby limit the reaction efficiency [40]. Likewise, for directly accessing the more twisted *sym-o*-bTAA, starting from 2-iodoaniline (**1b**) with arylboronic acid(ester)s **2** and aryl bromides **3** and after optimization of the SBH sequence (for details, see supporting information (SI)), 11 derivatives of *sym-o*-bTAA **5** are obtained after purification in yields ranging from 24 to 98% (Scheme 1).

The Suzuki step enables the reliable conversion of a broad spectrum of arylboronic acid(ester)s **2**, encompassing substituents from electron-donating to electron-withdrawing groups. In addition, the Buchwald–Hartwig amination tolerates a broad range of electronically diverse aryl bromides **3**, including sterically demanding substituents and heterocycles.

However, the *sym-m*-bTAA **4a-b** and **4q-r** as well as the *sym-o*-bTAA **5e**, **5k,** and **5m-n** represented exceptions, as they could only be accessed via a two-step synthesis (Scheme 2). In these cases, *sym-m*/*o*-bromo-substituted TAA (*sym-m*/*o*-Br-TAA) **6** is prepared in the first step according to a literature procedure (see SI) [41], which are then transformed into the products **4** or **5** under the established Suzuki conditions in yields ranging from 38 to 98%.

To our delight, upon employing equistoichiometric amounts of aryl bromides **3** in the amination step, a subsequent amination step with another aryl bromide **3** leads to an expansion of the SBH sequence into a four-component Suzuki–Buchwald–Hartwig/Buchwald–Hartwig ($S(BH)^2$) synthesis as selective access to unsymmetrically (*unsym-*) *N*,*N*-substituted derivatives *unsym-m*-bTAA **7** and *unsym-o*-bTAA **8** with yields ranging from 34 to 97% (Scheme 3).

2.2 | Structure

The unambiguous structural assignment of all TAA products **4–8** is based on extensive nuclear magnetic resonance (NMR) spectroscopy, mass spectrometry, and infrared (IR) spectroscopy (see SI). In addition, the molecular composition of the new compounds is confirmed by combustion analysis or high-performance liquid chromatography with human resource management system (see SI). Products of *sym-o*-bTAA bearing the strongly electron-releasing Me_2N substituents at positions R^1 or R^2 are indeed obtained and confirmed by mass spectrometry; however, the compounds are highly sensitive to oxidative decomposition. Furthermore, crystal structure analyses of *sym-o*-bTAA **5** were carried out to additionally confirm the molecular structure and the twisting of *para-* to *ortho*-bTAA [42].

X-ray crystallographic analysis of *sym-o*-bTAA **5** was performed on four selected derivatives (**5c**, **5g**, **5n,** and **5m**), with two of the crystals each comprising two molecules in the asymmetric unit (Figure 2). From the geometries, bond lengths *x*, C—N—C bond angles β, and torsion angles α were extracted, which, due to the twisting, can each be divided into multiple values (Table 1 and SI, chpt. 4).

The C—C bond lengths of the biaryl units (1.482–1.488 Å) are longer than the more polar C—N bonds x_2–x_4 (1.406–1.436 Å), and x_1 expectedly matches the corresponding biaryl unit in *sym-p*-bTAA (1.486 Å) [43]. The *ortho*-compounds **5** tend to exhibit longer C—N distances x_2 (1.421–1.436 Å) than both unsubstituted *sym-p*-bTAA (1.421 Å) [43] and TPA (∅1.420 Å) [44], which is attributed to steric repulsion between aryl rings 1 and 3. This also results in larger torsion angles α_1 (49°–62°) in *ortho*-linkages compared to the unsubstituted *sym-p*-bTAA (23°) [43]. The C—N bond lengths x_3 and x_4 range from 1.432 to 1.407 Å, without any discernible influence of the substitution pattern. In derivatives **5c**, **5g**, **5n**, **5m**, and unsubstituted *sym-p*-bTAA, the *C–N-C* bond angles β_1–β_3 fall within 116°–123°, closely matching the value observed for TPA (120°) [44]. In unsubstituted *sym-p*-bTAA, torsion angles α_2–α_4

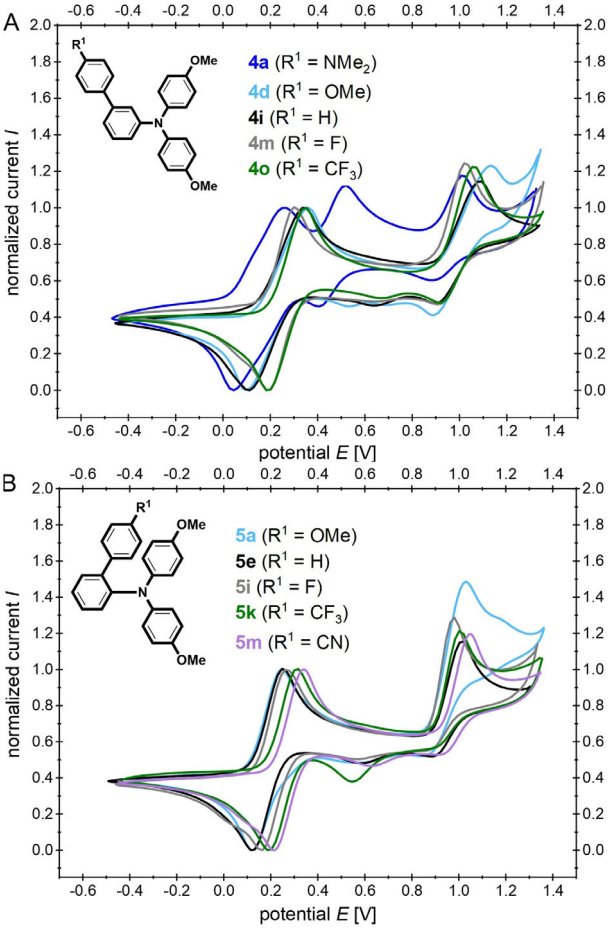

FIGURE 4 | Cyclic voltammograms of *sym-m*-bTAA **4a**, **4d**, **4i**, **4m,** and **4o** (**A**) and *sym-o*-bTAA **5a**, **5e**, **5i**, **5k,** and **5m** (**B**) with a variously substituted biaryl moiety R^1 in comparison (R^2 = OMe, recorded in CH_2Cl_2, T = 293 K, v = 100 mV/s, electrolyte: [$^nBu_4N$][PF_6], Pt working electrode, Pt counter electrode, Ag/AgCl reference electrode, redox standard: decamethylferrocene $E_0^{0/+1} = -0.54$ V (vs. ferrocene $E_0^{0/+1} = 0.00$ mV [45])).

(38°–46°) are relatively consistent, yet, unlike TPA (∅42°) [44], exhibit slight variations, while the *sym*-*o*-bTAA **5** displays much larger deviations (16°–74°). These distortions arise from steric repulsion between aryl rings 1 and 3, predominantly affecting α_3 but also influencing α_2 and α_4. Consequently, *ortho*-substitution (**5c**, **5g**, **5n,** and **5m**) significantly enhances the twisting of both the biaryl units (1 and 2) and the aryl substituents (2 and 4) at nitrogen, in comparison with *para*-substitution.

2.3 | Electrochemical Properties

The electronic ground state can be characterized by cyclic voltammetry, which was recorded in dichloromethane solutions at room temperature and redox potentials were referenced to ferrocene $E_0^{0/+1} = 0.00$ mV [45]. Cyclic voltammograms of *sym*-*m*-bTAA **4f-g**, **4k-l**, **4n**, and **4p-r** as well as *sym*-*o*-bTAA **5c**, **5g**, **5j**, **5l**, and **5n** exhibit an atypical behavior during the

TABLE 3 | Selected electrochemical properties ($E_0^{0/+1}$, $E_0^{+1/+2}$, and $E_0^{+2/+3}$, semiquinone formation constant K_{SEM}) of (*un*)*sym*-*m*-bTAA **4/7** and (*un*)*sym*-*o*-bTAA **5/8**.

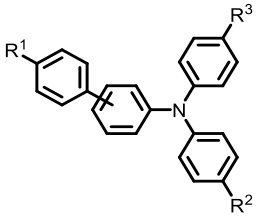

Compound	R^1	R^2	R^3	$E_0^{0/+1}$, V[a]	$E_0^{+1/+2}$, V[a]	$E_0^{+2/+3}$, V[a]	K_{SEM}[b]
4a	NMe_2	OMe	OMe	0.21	0.46	0.93	$1.66 \cdot 10^4$
4b	NMe_2	H	H	0.35	0.61	—[c]	$2.48 \cdot 10^4$
4c	OMe	NMe_2	NMe_2	−0.26	0.13	0.44	$5.18 \cdot 10^6$
4d	OMe	OMe	OMe	0.23	1.01	—	$1.50 \cdot 10^{13}$
4e	OMe	^{t}Bu	^{t}Bu	0.36	—[c]	—	—
4h	H	NMe_2	NMe_2	−0.25	0.16	1.09	$8.47 \cdot 10^6$
4i	H	OMe	OMe	0.24	0.95	—	$3.26 \cdot 10^{12}$
4j	H	^{t}Bu	^{t}Bu	0.38	0.43	—	—
4m	F	OMe	OMe	0.25	0.96	—	$1.05 \cdot 10^{12}$
4o	CF_3	OMe	OMe	0.27	0.98	—	$9.27 \cdot 10^{11}$
4s	OMe	Ph	Ph	0.45	—[c]	—	—
4t	OMe	Indol	Indol	−0.02	0.48	—	$2.66 \cdot 10^8$
5a	OMe	OMe	OMe	0.19	0.96	—	$7.35 \cdot 10^{12}$
5b	OMe	^{t}Bu	^{t}Bu	0.36	—[c]	—	—
5d	OMe	F	F	0.57	—[c]	—	—
5e	H	OMe	OMe	0.20	0.96	—	$7.76 \cdot 10^{12}$
5f	H	^{t}Bu	^{t}Bu	0.39	—[c]	—	—
5hr	H	F	F	0.57	—[c]	—	—
5i	F	OMe	OMe	0.22	0.91	—	$4.27 \cdot 10^{11}$
5k	CF_3	OMe	OMe	0.25	0.96	—	$1.06 \cdot 10^{12}$
5m	CN	OMe	OMe	0.27	0.97	—	$9.00 \cdot 10^{11}$
5o	OMe	Ph	Ph	0.46	—[c]	—	—
7c	H	OMe	CF_3	0.53	—	—	—
8c	H	OMe	CF_3	0.49	—[c]	—	—
8d	CF_3	OMe	H	0.39	—[c]	—	—

[a]Recorded in CH_2Cl_2, $T = 293$ K, extrapolation of data with v = 100, 250, 500, and 1000 mV/s to 0.00 mV/s, electrolyte: [^{n}Bu$_4$N][PF$_6$], Pt working electrode, Pt counter electrode, Ag/AgCl reference electrode, $E_0 = \frac{(E_{pa} - E_{pc})}{2}$ with redox standard: decamethylferrocene $E_0^{0/+1} = -0.54$ V (vs. ferrocene $E_0^{0/+1} = 0.00$ mV [45]).

[b]Semiquinone formation constant $K_{SEM} = 10^{\frac{E_0^{+1/+2} - E_0^{0/+1}}{0.059V}}$.

[c]Outside the measuring range.

measurements, since in multisweep experiments after the second cycle two redox processes of different magnitudes appear (Figure 3).

This redox behavior resembles the proposed irreversible oxidation of unsubstituted TPA as a result of dimerization to the corresponding benzidine [46]. In the first anodic half-cycle, a radical cation presumably forms at $E_{pa,2}$ (0.33–0.77 V), which undergoes dimerization at the electrode with concomitant aromatizing deprotonation, followed by stepwise twofold oxidation (Scheme 4). In this process, the second oxidation of the dimer and the first oxidation of the monomer bTAA overlap in a single intense signal at $E_{pa,2}$ (Figure 3) [46].

In the cathodic half-cycle, two successive reductions are observed at $E_{pc,1}$ (0.28–0.61 V) leading to the dimer radical and at $E_{pc,2}$ (0.13–0.43 V) yielding the neutral dimer. After the second cycle, a weak additional potential at $E_{pa,1}$ (0.12–0.42 V) grows in the anodic half-cycle and gradually increases in intensity with the number of cycles, while the intensity of $E_{pa,2}$ diminishes (see SI, chpt. 5.1, Figure S93). This can be explained by the increasing formation of the dimer at the expense of the monomer. For the monomer, a half-wave potential $E_0^{0/+1}$ (0.31–0.63 V) can still be estimated, and for the dimer both $E_0^{0/+1}$ (0.12–0.42 V) and $E_0^{+1/+2}$ (0.25–0.63 V) are discernible. Such processes were not observed for the *p*-bTAA, which is indicative of the stability of the in situ formed radical cation (Table 2) [39]. As for *sym-m*/*o*-bTAA **4** and **5**, some *unsym-m*/*o*-bTAA **7** and **8** also tend to undergo dimerization.

As shown in Table 2, all (*un*)*sym-m*-bTAA bearing an H or F substituent at R^2/R^3 exhibit a propensity to undergo oxidative dimerization, with the single exception of compound **4q**. In the absence of a resonance-stabilizing donor at R^2/R^3, dimerization is very likely favored. For compound **4b**, dimerization is probably suppressed by the presence of the strongly electron-donating NMe_2 substituent at R^1, while in **4q** the CN group appears to destabilize the radical cation sufficiently and a dimerization takes place even in the presence of a donor at R^2. By contrast, only (*un*)*sym-o*-bTAA **5** and **8** bearing at least one phenyl substituent on the central nitrogen atom exhibit a propensity for dimerization. This process is likely to occur at the *para*-position of a phenyl substituent within the TAA unit, as no dimerization is observed for compounds bearing substituents at R^2/R^3.

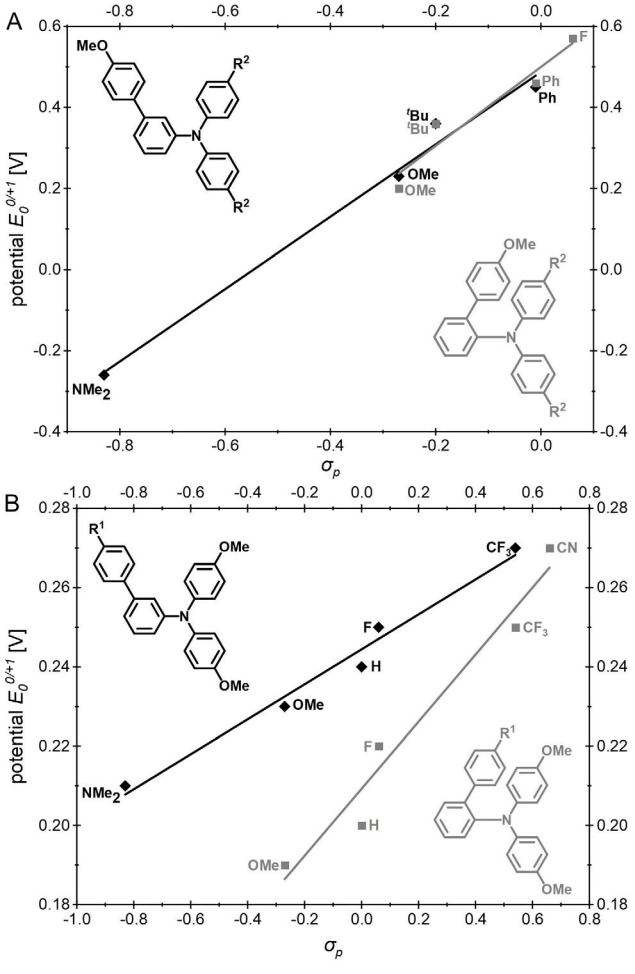

FIGURE 5 | 2D Correlation of $E_0^{0/+1}$ of *sym-m*-bTAA **4** and *sym-o*-bTAA **5** with the substituent parameter σ_p (**A**) with R^1 = OMe (*sym-m*-bTAA **4**: $E_0^{0/+1} = 0.892\,V \cdot \sigma_p + 0.487\,V$, $r^2 = 0.988$; *sym-o*-bTAA **5**: $E_0^{0/+1} = 0.973\,V \cdot \sigma_p + 0.500\,V$, $r^2 = 0.927$) and (**B**) with R^2 = OMe (*sym-m*-bTAA **4**: $E_0^{0/+1} = 0.044\,V \cdot \sigma_p + 0.244\,V$, $r^2 = 0.979$; *sym-o*-bTAA **5**: $E_0^{0/+1} = 0.085\,V \cdot \sigma_p + 0.209\,V$, $r^2 = 0.960$).

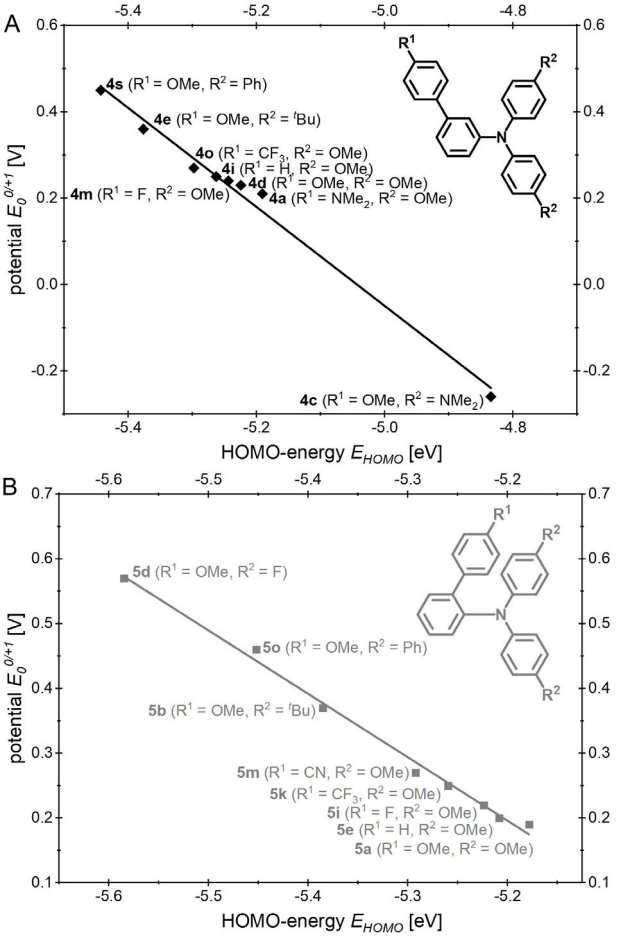

FIGURE 6 | 2D Correlation of $E_0^{0/+1}$ of methoxy-substituted (**A**) *sym-m*-bTAA **4** and (**B**) *sym-o*-bTAA **5** with the DFT-calculated HOMO energies E_{HOMO} (Gaussian 16, PBE1PBE/6-31+G**, PCM CH_2Cl_2, (**A**) *sym-m*-bTAA **4**: $E_0^{0/+1} = 1.173 \cdot E_{HOMO} - 5.912$ [V], $r^2 = 0.988$; (**B**) *sym-o*-bTAA **5**: $E_0^{0/+1} = -0.956 \cdot E_{HOMO} - 4.775$ [V], $r^2 = 0.998$).

TABLE 4 | Selected photophysical properties (absorption maxima in solution with absorption coefficients ε and emission maxima in solution and in the solid state with fluorescence quantum yields Φ_F and Stokes shifts $\delta\tilde{\nu}_S$) of (*un*)*sym*-*m*-bTAA **4/7** and (*un*)*sym*-*o*-bTAA **5/8**.

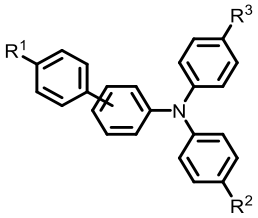

Compound	R^1	R^2	R^3	$\lambda_{max,abs}$, nm[a] (ε, m^{-1} cm^{-1})	$\lambda_{max,em\ (solution)}$, nm[b] ($\Phi_F$)[c]	$\Delta\tilde{\nu}_S$, cm^{-1}[d]	$\lambda_{max,em(solid)}$, nm[e] (Φ_F)[f]
4a	NMe_2	OMe	OMe	306 (51 500), 365 (sh, 2300)	428 (0.02)	4000	410 (0.09)
4b	NMe_2	H	H	305 (65 400)	381 (0.02)	6500	395 (0.01)
4c	OMe	NMe_2	NMe_2	264 (35 100), 311 (28100), 385 (sh, 1700)	524 (0.01)	6900	428 (0.04)
4d	OMe	OMe	OMe	271 (31 500), 293 (sh, 29 400), 360 (sh, 2100)	446 (0.02)	5400	414 (0.07)
4e	OMe	^{t}Bu	^{t}Bu	268 (sh, 33 500), 293 (34 900)	420 (0.02)	10 300	406 (0.05)
4f	OMe	H	H	270 (sh, 26 300), 287 (27 300), 347 (sh, 1900)	403 (0.02)	4000	397 (0.02)
4g	OMe	F	F	281 (20 000), 353 (sh, 3400)	388 (0.04)	2600	403 (0.01)
4h	H	NMe_2	NMe_2	255 (25 200), 331 (21 200)	548 (0.01)	12 000	472 (0.01)
4i	H	OMe	OMe	253 (24 900), 301 (23 900), 366 (sh, 1500)	465 (0.03)	5800	410 (0.02)
4j	H	^{t}Bu	^{t}Bu	251 (24 500), 303 (27 900)	434 (0.02)	10 000	401 (0.02)
4k	H	H	H	250 (23 200), 302 (25 500), 353 (sh, 1200)	417 (0.02)	4300	405 (0.03)
4l	H	F	F	257 (34 800), 295 (34 100), 350 (sh, 2800)	412 (0.02)	4300	360 (0.01)
4m	F	OMe	OMe	251 (24 800), 301 (24 400), 363 (sh, 1300)	455 (0.02)	5600	423 (0.02)
4n	F	H	H	248 (22 200), 302 (25 000), 351 (sh, 1400)	415 (0.02)	4500	391 (0.01)
4o	CF_3	OMe	OMe	258 (25 400), 301 (23 100), 371 (sh, 1600)	523 (0.03)	7800	468 (0.01)
4p	CF_3	H	H	252 (24 000), 264 (sh, 23 000), 301 (26 500), 356 (sh, 1500)	454 (0.05)	6100	417 (0.05)
4q	CN	OMe	OMe	281 (38 400), 379 (sh, 8700)	562 (0.01)	8600	471 (0.21)
4r	CN	H	H	262 (sh, 26 800), 286 (33 700), 360 (sh, 2200)	500 (0.05)	7800	469 (0.08)
4s	OMe	Ph	Ph	253 (34 400), 331 (37 600)	415 (0.17)	6100	427 (0.13)
4t	OMe	1-Ph-indol-5-yl	1-Ph-indol-5-yl	282 (20 000), 320 (sh, 10 700), 361 (sh, 22 000)	400 (0.05)	2700	—
5a	OMe	OMe	OMe	262 (20 500), 307 (23 000), 362 (sh, 2400)	434 (0.08)	4600	391 (0.02)
5b	OMe	^{t}Bu	^{t}Bu	257 (21200), 305 (29 700)	418 (0.11)	8800	394 (0.06)
5c	OMe	H	H	262 (18 600), 301 (23 500), 344 (sh, 2300)	400 (0.12)	4100	387 (0.06)

(Continues)

TABLE 4 | (Continued)

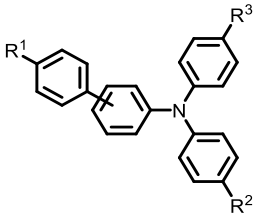

Compound	R^1	R^2	R^3	$\lambda_{max,abs}$, nm[a] (ε, m^{-1} cm^{-1})	$\lambda_{max,em\ (solution)}$, nm[b] ($\Phi_F$)[c]	$\Delta\tilde{\nu}_S$, cm^{-1}[d]	$\lambda_{max,em(solid)}$, nm[e] (Φ_F)[f]
5d	OMe	F	F	262 (20 400), 299 (24 400), 350 (sh, 2200)	394 (0.03)	3200	386 (0.04)
5e	H	OMe	OMe	239 (20 500), 306 (22 500), 363 (sh, 2400)	454 (0.13)	5500	412 (0.06)
5f	H	^{t}Bu	^{t}Bu	233 (19 000), 304 (24 000)	427 (0.21)	9500	413 (0.07)
5g	H	H	H	238 (18 100), 302 (20 800), 346 (sh, 1000)	408 (0.11)	4400	410 (0.05)
5h	H	F	F	236 (16 500), 298 (18 700), 351 (sh, 1800)	412 (0.05)	4200	437 (0.05)
5i	F	OMe	OMe	232 (19 400), 305 (19 800)	448 (0.13)	8900	413 (0.02)
5j	F	H	H	235 (17 200), 302 (21 500)	412 (0.11)	8900	396 (0.07)
5k	CF_3	OMe	OMe	266 (50 000), 304 (17 500), 367 (sh, 2300)	501 (0.20)	7300	485 (0.32)
5l	CF_3	H	H	235 (20 600), 302 (20 900), 359 (sh, 1900)	442 (0.08)	5100	433 (0.08)
5m	CN	OMe	OMe	269 (27 500), 307 (19 000), 388 (sh, 2100)	546 (0.16)	7500	486 (0.26)
5n	CN	H	H	260 (26 200), 295 (20 700), 354 (sh, 2900)	478 (0.45)	7300	423 (0.16)
5o	OMe	Ph	Ph	246 (35 800), 338 (43 200)	402 (0.55)	4700	412 (0.15)
7a	OMe	F	H	270 (sh, 45 800), 285 (48 700), 347 (sh, 2800)	393 (0.04)	3400	383 (0.05)
7b	OMe	H	CF_3	283 (22 800), 321 (sh, 12 300)	396 (0.08)	5900	384 (0.01)
7c	H	OMe	CF_3	258 (18 300), 303 (15 700)	425 (0.07)	9500	430 (0.05)
7d	CF_3	OMe	H	258 (20 800), 303 (17 700)	424 (0.02)	9400	421 (0.04)
8a	OMe	*p*-F	H	261 (20 300), 301 (24 500)	398 (0.11)	8100	385 (0.01)
8b	OMe	H	CF_3	262 (17 000), 305 (20 700)	388 (0.12)	7000	370 (0.05)
8c	H	*p*-OMe	CF_3	232 (21 100), 303 (20 000), 390 (sh, 1000)	418 (0.13)	7200	408 (0.08)
8d	CF_3	*p*-OMe	H	234 (19 300), 300 (18 500), 369 (sh, 1500)	468 (0.26)	12 000	442 (0.13)
8e	OMe	*o*-Me	H	300 (25 200)	399 (0.12)	8300	381 (0.12)
8f	OMe	1-Ph-indol-5-yl	H	266 (38 600), 313 (sh, 25 000)	423 (0.07)	8300	—

[a]Recorded in CH_2Cl_2, $T = 293$ K, $c = 10^{-5}$ M.
[b]Recorded in CH_2Cl_2, $T = 293$ K, $c = 10^{-7}$ M.
[c]Absolute quantum yields recorded in CH_2Cl_2, $T = 293$ K, $c = 10^{-6}$ M.
[d]$\Delta\tilde{\nu}_S = \frac{1}{\lambda_{max,abs}} - \frac{1}{\lambda_{max,em}}$.
[e]Recorded at $T = 293$ K.
[f]Absolute quantum yields recorded at $T = 293$ K.

All remaining (*un*)*sym*-*m*-bTAA **4** and **7** together with (*un*)*sym*-*o*-bTAA **5** and **8** with substituents at R^2/R^3 display reversible redox processes (Nernst behavior) in dichloromethane and can be classified as multistep Wurster-type redox systems (Figure 4). Their oxidation potentials $E_0^{0/+1}$ (−0.25–0.57 V) and $E_0^{+1/+2}$ (0.13–1.01 V) fall mostly into a similar range as those of the

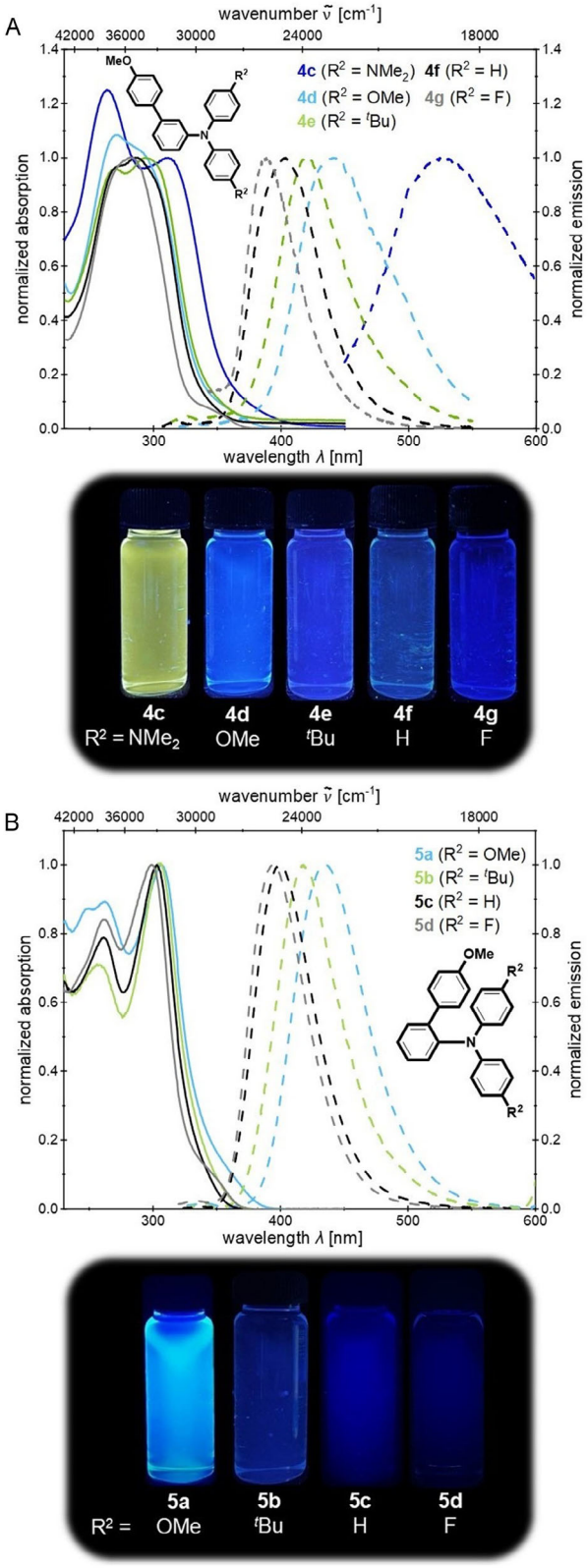

FIGURE 7 | Comparison of the UV/Vis absorption and emission spectra (above, absorption spectra recorded in CH_2Cl_2, $T = 293$ K, $c = 10^{-5}$ M (bold lines) and emission spectra recorded in CH_2Cl_2, $T = 293$ K, $c = 10^{-7}$ M (dashed lines)) and emission behavior (below, recorded in CH_2Cl_2, $T = 293$ K, $c = 10^{-7}$ M, $\lambda_{exc} = 365$ nm) of (**A**) *sym-m*-bTAA **4c-g** and (**B**) *sym-o*-bTAA **5a-d** with a constant substitution pattern at position R^1 = OMe.

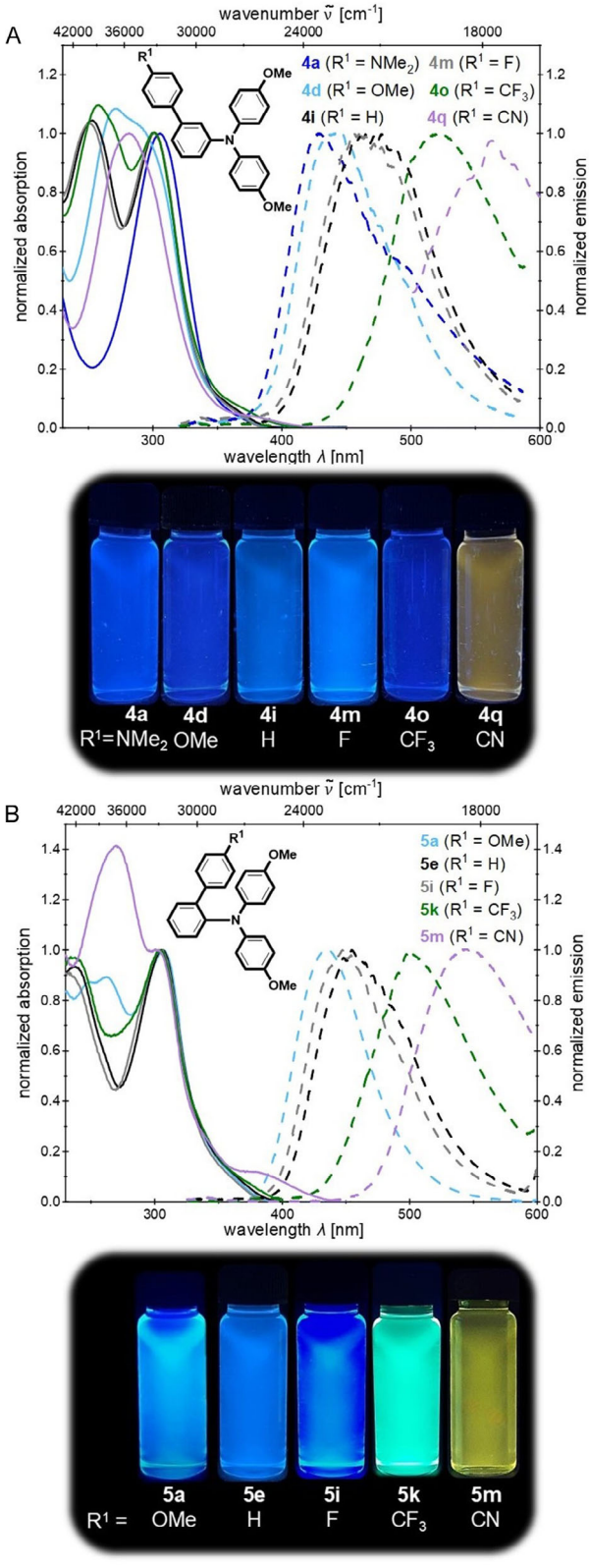

FIGURE 8 | Comparison of the UV/Vis absorption and emission spectra (above, absorption spectra recorded in CH_2Cl_2, $T = 293$ K, $c = 10^{-5}$ M (bold lines) and emission spectra recorded in CH_2Cl_2, $T = 293$ K, $c = 10^{-7}$ M (dashed lines)) and emission behavior (below, recorded in CH_2Cl_2, $T = 293$ K, $c = 10^{-7}$ M, $\lambda_{exc} = 365$ nm) of (**A**) *sym-m*-bTAA **4a**, **4d**, **4i**, **4m**, **4o**, **4q** and (**B**) *sym-o*-bTAA **5a**, **5e**, **5i**, **5k**, **5m** with a constant substitution pattern at position R^2 = OMe.

sym-p-bTAA with the same substitution pattern (Table 3) [39]. The potential differences, and hence the K_{SEM} values, resemble those of the *para*-analogues, showing that radical cations are comparably stable in the absence of dimerization pathways [39].

The $E_0^{0/+1}$ depends on the electronic nature of the functional group (Table 3). Strong donors stabilize the positive charge of the radical cation, facilitate oxidation, and induce a cathodic shift of the redox potentials, whereas acceptors cause anodic shifts. The relationship between $E_0^{0/+1}$ of the *sym-m/o*-bTAA **4** and **5**, which do not dimerize, and the electronic character of the substituents can be semiquantitatively described by two linear Hammett correlations. In the consanguineous series with R^1 or R^2 = OMe, $E_0^{0/+1}$ can be represented as a function of the electronic character of the substituent at the respective alternate position (Figure 5). Correlations of the experimentally determined values with the Hammett parameters (σ_p, σ_p^-, σ_p^+, σ_R, and σ_I) show the best agreement with the original Hammett parameter σ_p (see SI, chpt. 8) [47]. This suggests that both inductive and resonance effects of the substituents ($\sigma_p = \sigma_I + \sigma_R$) at R^1 and R^2 affect the oxidation to the cation, with the resonance effect exerting the stronger influence.

Comparison of the correlation equations (Figure 5) illustrates that R^2 exerts a stronger influence on $E_0^{0/+1}$, as indicated by the larger slope. Substituent R^2 is located closer to the central nitrogen atom and thus acts both by mesomerism and more strongly by inductive effects than R^1, which explains the good correlation with σ_p [47].

As evidenced by the excellent correlation coefficients r^2, the 2D SPR (Figure 5) demonstrate that $E_0^{0/+1}$ values of *sym-m/o*-bTAA **4** and **5** can be rapidly and empirically predicted for the substitution pattern at R^1 and R^2.

The prediction model derived from substituent parameters [47] can be further refined by quantum chemical approaches. Correlations between DFT-calculated HOMO energies E_{HOMO} and experimental $E_0^{0/+1}$ values of the methoxy-substituted *sym-m/o*-bTAA **4** and **5** exhibit excellent agreement (Figure 6), offering an additional basis for the rational design of tailored compounds **4** and **5** with precisely tunable electrochemical properties.

2.4 | Photophysical Properties

All bTAA dyes fluoresce in dichloromethane solution upon excitation with UV light with emission colors ranging from blue to yellow. Therefore, the electronic properties of all bTAA were investigated by UV/Vis absorption and static fluorescence spectroscopy (Table 4). The (*un*)*sym-m/o*-bTAA **4**, **5**, **7,** and **8** (except for **4a-b**, **4g**, **7b**, and **8e**) exhibit at least two significant absorption maxima in the UV region (232–283 nm and 285–361 nm) in dichloromethane with molar absorption coefficients ε ranging from 13 000 to 6500 m^{-1} cm^{-1}, which are responsible for the colorless solutions. Except for **4b**, **4e**, **4h**, **4j**, **4s**, **5b**, **5f**, **5i-j**, and **5o**, a weak shoulder appears between 344 and 388 nm (ε = 1000–8700 m^{-1} cm^{-1}), being most pronounced in acceptor-substituted derivatives (**4o-r** and **5k-n**).

Accordingly, the substitution pattern at R^1 and R^2 affects the positioning of the shoulder, yet quantitative analysis by Hammett correlation is precluded by experimental uncertainty. Since the shoulder is not always clearly discernible in the spectra, all spectra are normalized consistently to the preceding band.

Depending on the substituent, (*un*)*sym-m/o*-bTAA **4**, **5**, **7**, and **8** display fluorescence maxima between 381 and 562 nm upon photonic excitation, covering the spectral range from blue to yellow emission. Except for the heterocyclic compound **4t**, all derivatives also emit in the solid state (360–486 nm). Their emission behavior is therefore comparable to that of *sym-p*-bTAA with analogous substitution patterns [39]. Absolute fluorescence quantum yields reach up to 55% in dichloromethane and 26% in the solid state, which is lower than those of *sym-p*-bTAA [39]. In solution, the emission maximum can be tuned by the electronic nature of the substituents, both through the *para*-position R^1 and through R^2 of the aryl rings (Figures 7 and 8). This relationship is first

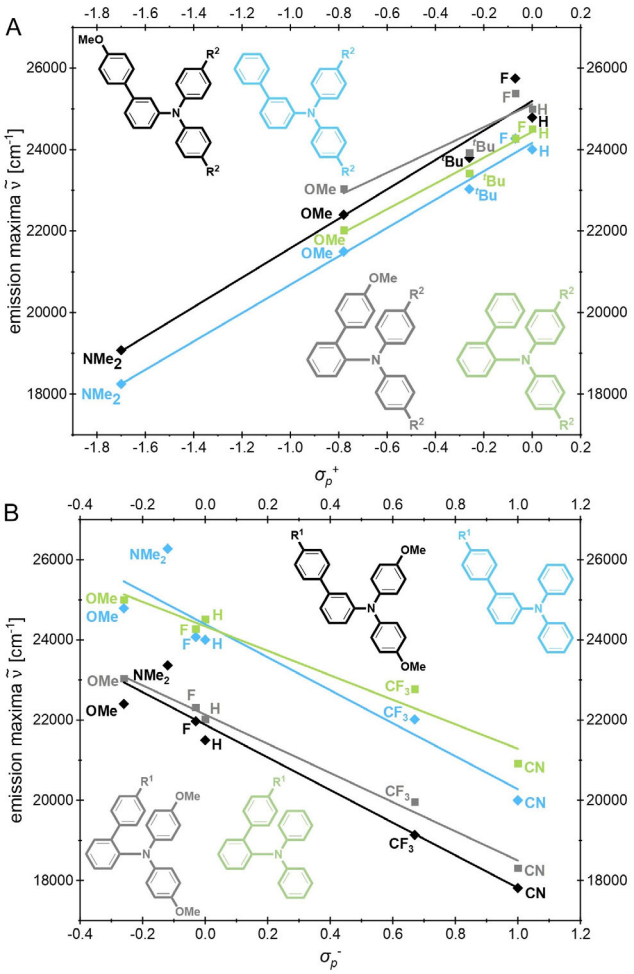

FIGURE 9 | 2D Correlation of emission maxima $\tilde{\nu}_{max,em}$ of *sym-m*-bTAA **4** (black/blue) and *sym-o*-bTAA **5** (gray/green) with (**A**) the substituent parameter σ_p^+ with R^1 = const. (*sym-m*-bTAA **4** (R^1 = OMe): $\tilde{\nu}_{max,em} = 3611 \cdot \sigma_p^+ + 25192$ [cm^{-1}], $r^2 = 0.977$; *sym-m*-bTAA **4** (R^1 = H): $\tilde{\nu}_{max,em} = 3481 \cdot \sigma_p^+ + 24167$ [cm^{-1}], $r^2 = 0.992$; *sym-o*-bTAA **5** (R^1 = OMe): $\tilde{\nu}_{max,em} = 2801 \cdot \sigma_p^+ + 25114$ [cm^{-1}], $r^2 = 0.866$; *sym-o*-bTAA **5** (R^1 = H): $\tilde{\nu}_{max,em} = 3163 \cdot \sigma_p^+ + 24435$ [cm^{-1}], $r^2 = 0.996$) and (**B**) the substituent parameter σ_p^- with R^2 = const. (*sym-m*-bTAA **4** (R^2 = OMe): $\tilde{\nu}_{max,em} = 4067 \cdot \sigma_p^- + 21883$ [cm^{-1}], $r^2 = 0.936$; *sym-m*-bTAA **4** (R^2 = H): $\tilde{\nu}_{max,em} = -4113 \cdot \sigma_p^- + 24390$ [cm^{-1}], $r^2 = 0.879$; *sym-o*-bTAA **5** (R^2 = OMe): $\tilde{\nu}_{max,em} = -3639 \cdot \sigma_p^- + 22138$ [cm^{-1}], $r^2 = 0.992$; *sym-o*-bTAA **5** (R^2 = H): $\tilde{\nu}_{max,em} = -3054 \cdot \sigma_p^- + 24339$ [cm^{-1}], $r^2 = 0.960$).

detailed for the dependence on electronic effects in the consanguineous series with a constant substituent at position R^1 and varying substituents at position R^2 (Figure 7).

The emission maxima shift hypsochromically with decreasing donor character of R^2. The plot of the experimental emission maxima against various Hammett parameters shows an excellent correlation with σ_p^+ (Figure 9(A)) [47]. This suggests mesomeric stabilization of the vibrationally relaxed S_1 state by electron-donating groups, while electron-withdrawing groups act destabilizingly and lead to a hypsochromic shift. The plot thus results in a positive correlation, as the wavenumber increases with increasing acceptor character, i.e., with increasing σ_p^+. The comparable slopes of the emission correlations with σ_p^+ for R^2 in the *meta*-bTAA **4**, *ortho*-bTAA **5**, and *para*-bTAA [39] indicate a similar electronic influence on the excited state.

In addition, the electronic effects within the consanguineous series bearing a constant substituent at R^2 and variable substituents at R^1 are to be analyzed in detail and systematically delineated (Figure 8).

In contrast to the series with varying R^2, the emission maxima shift bathochromically with decreasing donor character of R^1. The emission maxima correlate excellently with σ_p^-, indicating mesomeric stabilization of the vibrationally relaxed S_1 state by electron-withdrawing groups at R^1 (Figure 9 (**B**)). Unlike the *sym-p*-bTAA [39], compounds **4a** and **4b** with an NMe_2 group at R^1 do not systematically deviate from this behavior. Overall, a negative correlation is obtained, since the wavenumber decreases with increasing acceptor character, i.e., with increasing σ_p^-. The emission correlation with σ_p^- shows steeper slopes for *sym-m*-bTAA **4** and similar slopes for *sym-o*-bTAA **5** compared to *sym-p*-bTAA [39], suggesting a somewhat stronger influence of R^1 in *meta*-biaryl twisting.

In the emission correlations, the substituent parameters σ_I and σ_R generally afford lower r^2 values across all consanguineous series, with σ_R consistently providing stronger correlations, underscoring the dominant role of the resonance effect (see SI). The resulting Hammett correlations, exhibiting excellent correlation coefficients ($r^2 = 0.866–0.996$), demonstrate that rational design

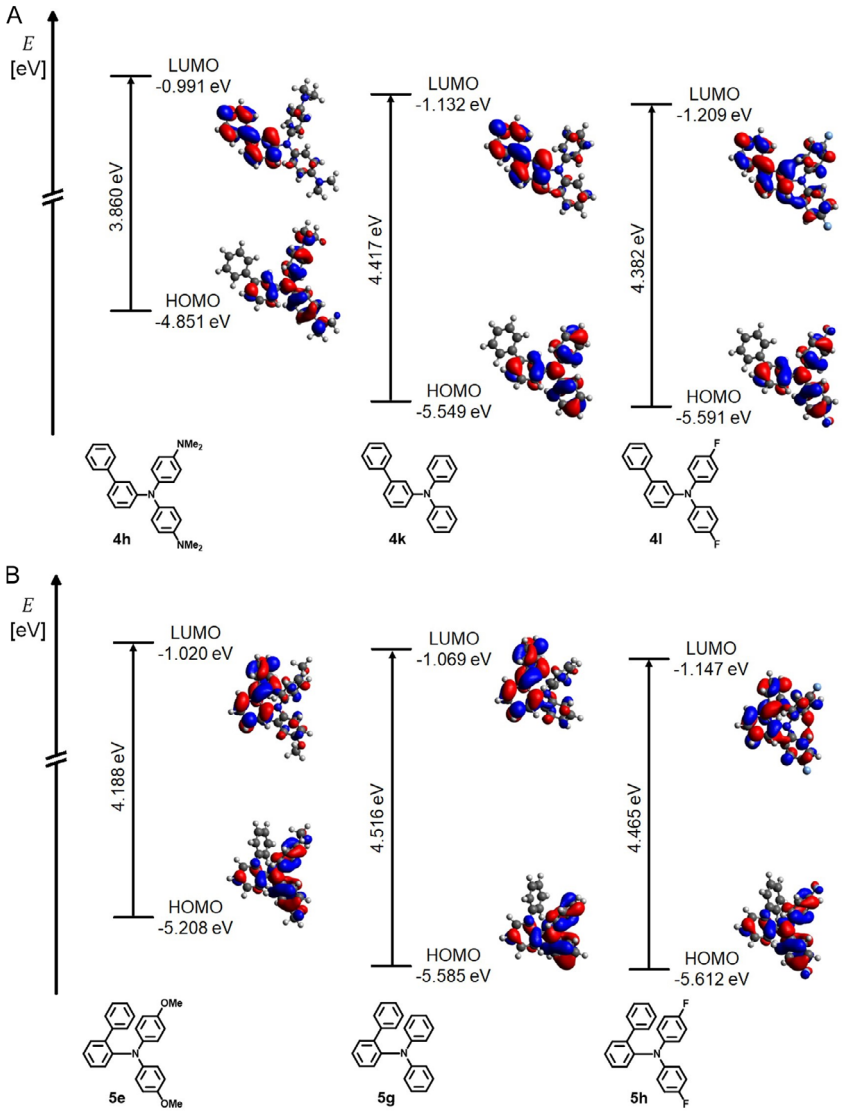

FIGURE 10 | Selected Kohn–Sham FMO of (**A**) *sym-m*-bTAA **4h**, **4k** and **4l**, and (**B**) *sym-o*-bTAA **5e**, **5g,** and **5h** (Gaussian 16, PBE1PBE/6-31+G**, PCM CH_2Cl_2, isosurface value at 0.025 a.u.). FMO = Frontier molecular orbitals.

of tailored *sym-m*/*o*-bTAA **4** and **5** with specifically tunable emission properties is achievable.

The Stokes shift $\tilde{\nu}_S$ also shows a dependence on the substituents but cannot be quantified due to the uncertainty in determining the longest wavelength absorption shoulder. Plots of the absolute fluorescence quantum yield Φ_F against the parameters likewise revealed no significant correlations, suggesting that Φ_F cannot be described solely by substituent effects [47]. The substitution pattern also influences the position of the solid-state emission maxima, but no correlation with Hammett parameters is evident. Solid-state emission is likely to be dominated by intermolecular interactions rather than purely molecular electronic substituent effects, as molecular packing in the solid state significantly influences the electronic states. The fluorescence quantum yield Φ_F in the solid state is lower than in solution, which can be explained by the nonradiative reabsorption of photons in the solid state [48].

2.5 | Calculated Electronic Structure

For deeper insights into the electronic structures of bTAA, time-dependent density functional theory (TD-DFT) calculations were performed using Gaussian 16 [49]. Analogous to the *sym-p*-bTAA [39], the PBE1PBE functional [50, 51] and the Pople basis set 6-31+G* [52] were employed. All minimum structures were confirmed by analytical frequency analysis (NImag = 0). Consistent with the spectroscopic properties, the calculations were carried out using the polarizable continuum model (PCM) with dichloromethane as the dielectric medium [53]. Exemplarily, H-substituted derivatives **4** and **5** were investigated (see SI, chpt. 7.1, Table S12 and S13). The calculated excitation and emission energies agree satisfactorily with the experimental data. The calculated absorption spectra of **4k** and **4g** reveal that the respective absorption bands consist of several transitions, which merge into broad bands due to line broadening (see SI, chpt. 7.1, Figure S228 and S234). The higher-energy band predominantly exhibits locally excited (LE) character with high oscillator strength *f*, whereas the

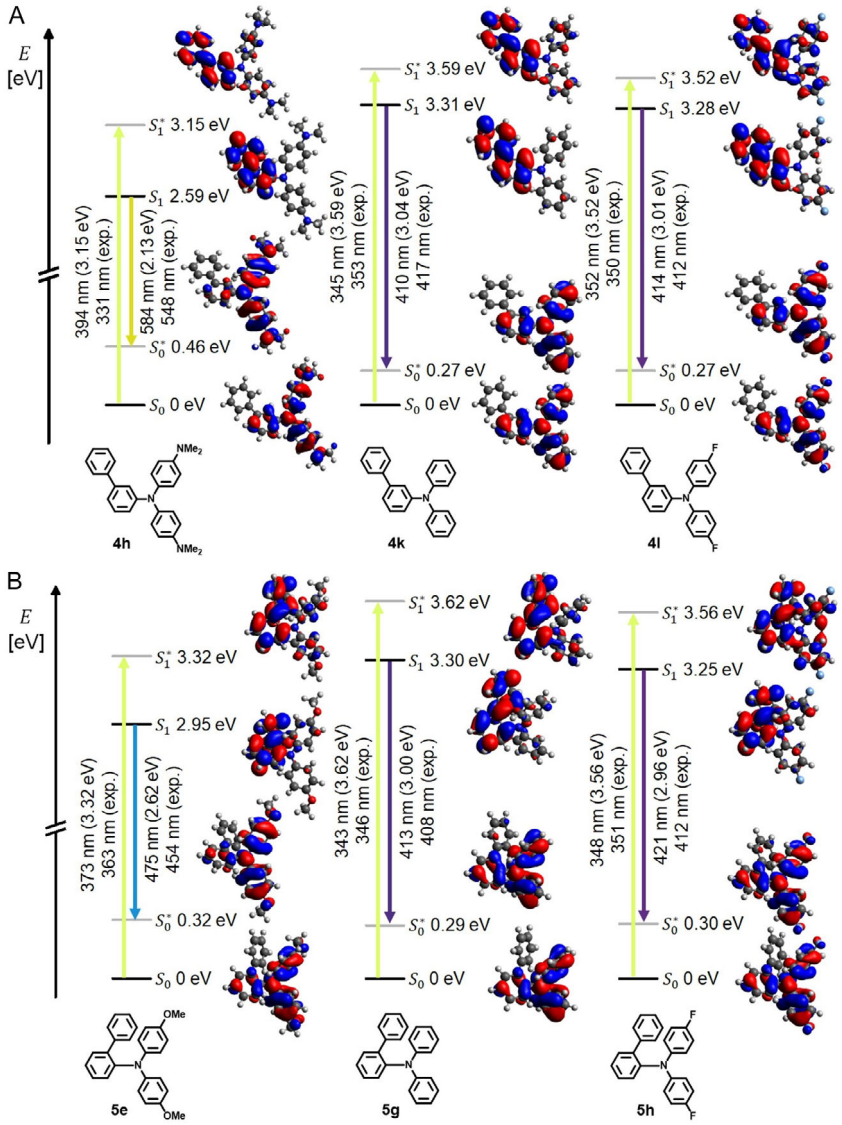

FIGURE 11 | TD-DFT-computed Jabłoński diagrams and Kohn–Sham FMO corresponding to the S_0-S_1*-transition (longest wavelength absorption) and the S_1-S_0*-transition (fluorescence) of (**A**) *sym-m*-bTAA **4h**, **4k,** and **4l**, and (**B**) *sym-o*-bTAA **5e**, **5g,** and **5h** (Gaussian 16, PBE1PBE/6-31+G**, PCM CH_2Cl_2, isosurface value at 0.025 a.u.). TD-DFT = Time-dependent density functional theory; FMO = frontier molecular orbitals.

longest wavelength band, including the HOMO → LUMO transition, is characterized by charge–transfer (CT) character with low *f*. In comparison, the unsubstituted *sym-p*-bTAA is dominated by the HOMO → LUMO transition with high *f* due to efficient *para*-conjugation and pronounced electron delocalization [39, 54]. By contrast, the HOMO → LUMO transitions of the *meta*- and *ortho*-isomers **4k** and **5g** are significantly weaker and in some cases appear only as a small longest wavelength shoulder. Nevertheless, the *f* value of the *sym-o*-bTAA **5** is higher than that of the *sym-m*-bTAA **4**, which can be attributed to the particularly unfavorable conjugation of the *meta*-substitution.

The effect of the aryl substituent R^2 on the luminophore framework was examined using the consanguineous series **4hr-l** and **5e-h**, bearing a constant substituent at R^1 (= H) in the biaryl fragment (Figure 10). TD-DFT calculations indicate that the $S_0 \rightarrow S_1$ transition can be approximated as a HOMO → LUMO transition (≥93% contribution). Similar to *sym-p*-bTAA [39], the HOMO energy decreases with reduced donor strength, while the effect on the LUMO is comparatively minor. The calculated frontier molecular orbitals (FMO) reveal HOMO density localized on the TAA core, whereas LUMO density extends into the biaryl moiety (Figure 10). Thus, photoexcitation is accompanied by a slight CT from the TAA to the biaryl unit. As the donor character diminishes, this CT character decreases and electron density becomes more delocalized over the entire π-system, leading rather to LE character (see **8hr**, Figure 10). This effect is particularly evident in *ortho*-derivatives, presumably due to the spatial proximity of biaryl and TAA moieties, which enables stronger orbital overlap. In **4i**, **4k-l**, **5e**, and **5g-h**, excitation into the S_1* state is revealed experimentally as a red-shifted shoulder, whereas in donor-substituted derivatives **4hr**, **4j**, and **5f,** the transition overlaps with the preceding maximum, precluding reliable Hammett correlations. However, TD-DFT calculations yielded the energy gap between HOMO and LUMO $\Delta E(E_{HOMO}$-$E_{LUMO})$, which can be interpreted as the theoretical longest wavelength absorption band without overlap. Correlation with σ_p^+ (see SI, chpt. 7.1, Figure S229 and S235) gives excellent coefficients ($r^2 = 0.998$ (**4h-l**) and $r^2 = 0.989$ (**5e-h**)). The positive

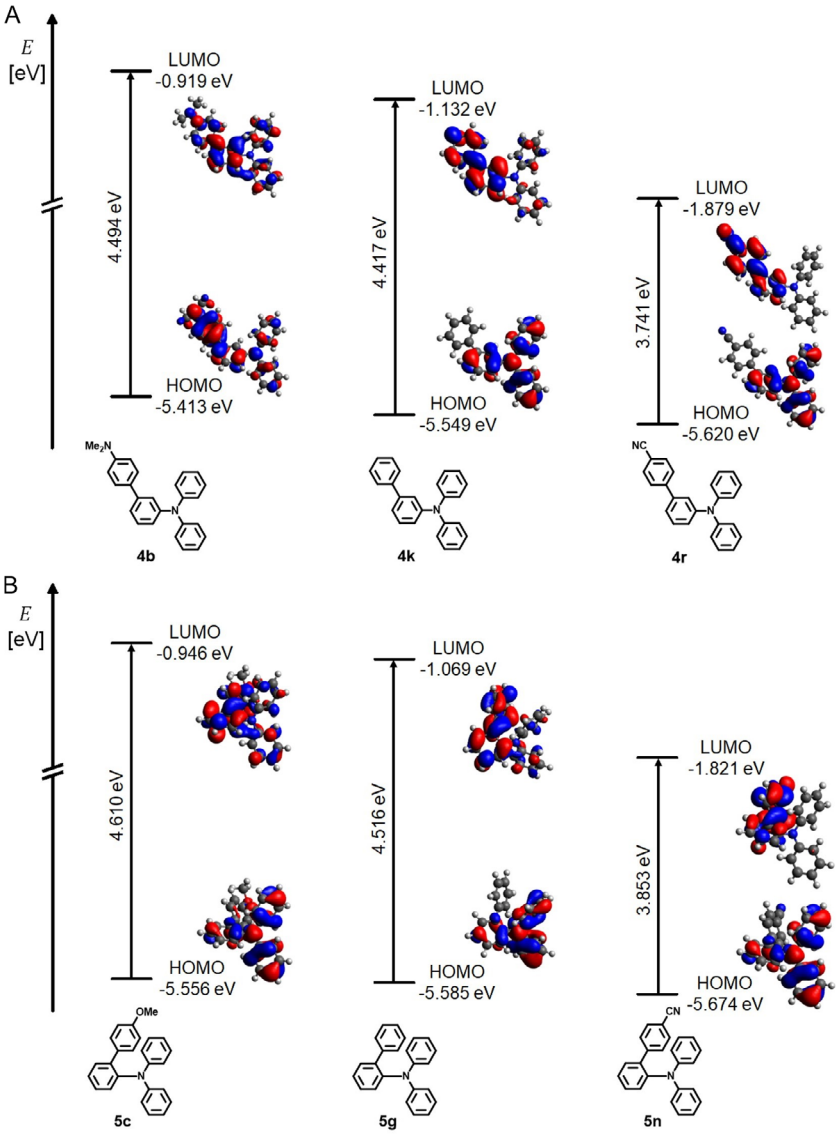

FIGURE 12 | Selected Kohn–Sham FMO of (**A**) *sym-m*-bTAA **4b**, **4k,** and **4r**, and (**B**) *sym-o*-bTAA **5c**, **5g,** and **5n** (Gaussian 16, PBE1PBE/6-31+G**, PCM CH_2Cl_2, isosurface value at 0.025 a.u.). FMO = Frontier molecular orbitals.

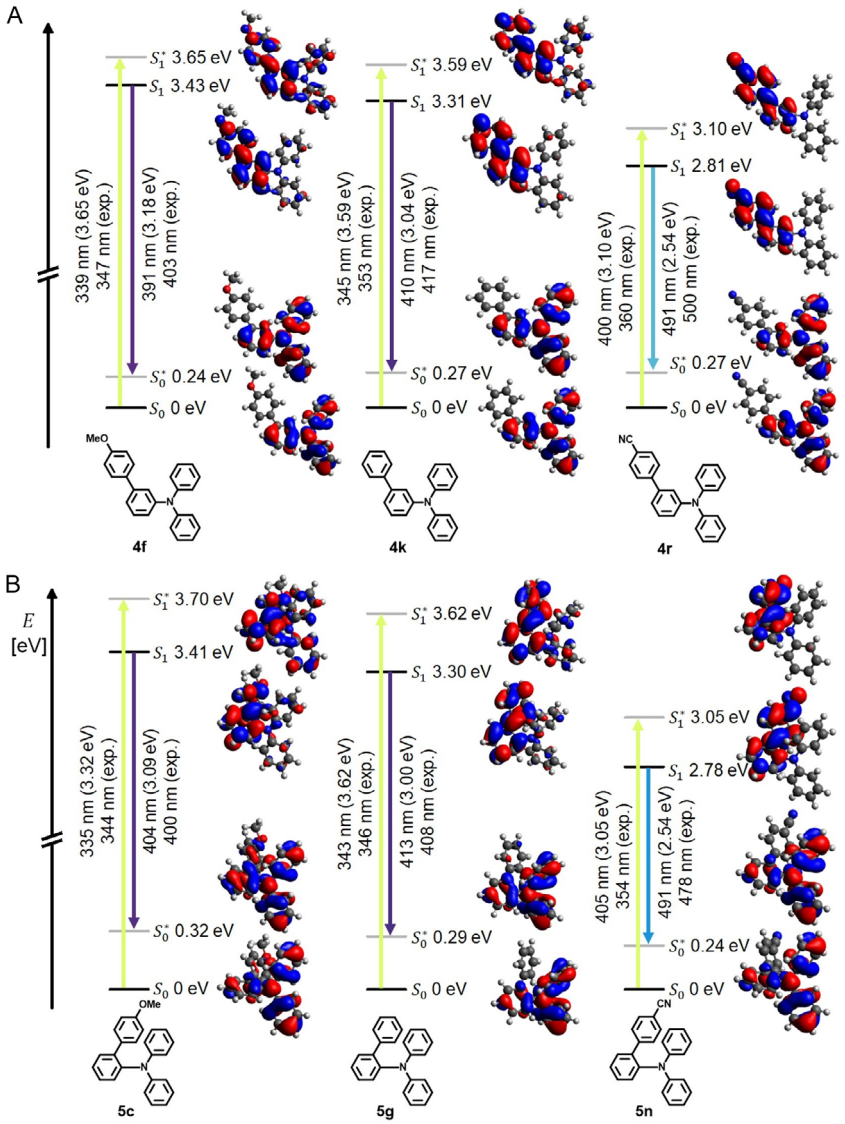

FIGURE 13 | TD-DFT-computed Jabłoński diagrams and Kohn–Sham FMO corresponding to the S_0-S_1*-transition (longest wavelength absorption) and the S_1-S_0*-transition (fluorescence) of (**A**) *sym-m*-bTAA **4f**, **4k,** and **4r**, and (**B**) *sym-o*-bTAA **5c**, **5g,** and **5n** (Gaussian 16, PBE1PBE/6-31+G**, PCM CH_2Cl_2, isosurface value at 0.025 a.u.).

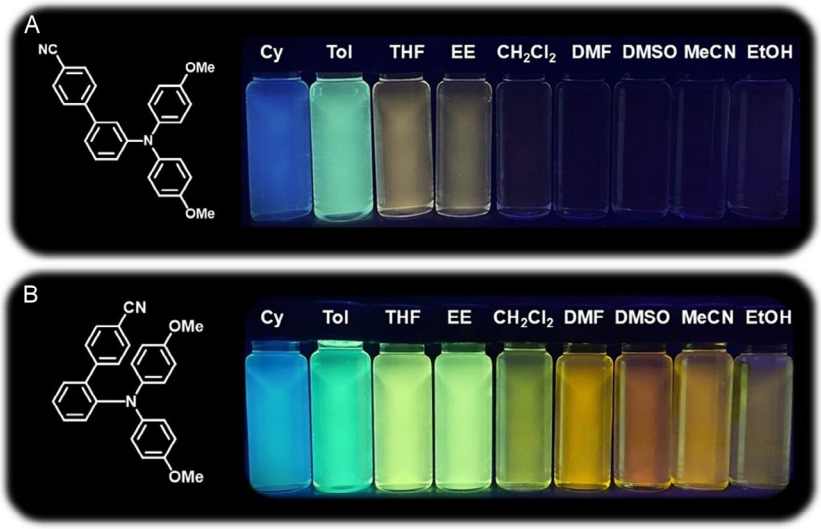

FIGURE 14 | Emission solvatochromism of (**A**) *sym-m*-bTAA **4q** and (**B**) *sym-o*-bTAA **5m** (from left to right: cyclohexane, toluene, THF, EtOAc, CH_2Cl_2, DMF, DMSO, MeCN, EtOH; $\lambda_{exc} = 356$ nm, $T = 298$ K, $c = 10^7$ M).

correlation indicates that the longest wavelength absorption shifts hypsochromically with decreasing donor strength of R^2. Donor substituents at R^2 reduce $\Delta E(E_{HOMO}\text{-}E_{LUMO})$ through resonance by destabilizing the HOMO.

Comparison of the Jabłoński diagrams (Figure 11) illustrates that the energy of the S_1* state increases with decreasing donor strength at R^2. In the excited state, electron-donating substituents at R^2 stabilize the electron density, as the LUMO coefficient density is localized on the biaryl unit. With decreasing donor character, the emission maximum shifts hypsochromically, which is consistent with the experimental data. Accordingly, the linear correlation of the calculated emission maxima with σ_p^+ shows the highest agreement ($r^2 = 0.999$ (**4h-l**) and $r^2 = 0.996$ (**5e-h**)) (see SI, chpt. 7.1, Figure S230 and S236).

The energy difference between the vibrationally excited and vibrationally relaxed states increases in derivatives with strong donors **4h** and **5e**, resulting in a larger Stokes shift $\tilde{\nu}_S$ (Figure 11). Plotting the quantum-chemically calculated Stokes shift $\tilde{\nu}_{S,calcd}$ against σ_p^+ reveals excellent correlations ($r^2 = 0.985$ (**4h-l**) and $r^2 = 0.998$ (**5e-h**)) (see SI, chpt. 7.1, Figure S231 and S237), emphasizing enhanced molecular relaxation induced by electron-donating substituents at R^2.

The influence of the aryl substituent R^1 in the consanguineous series of *sym-m*-bTAA **4b**, **4f**, **4k**, **4n**, **4p**, and **4r** as well as *sym-o*-bTAA **5c**, **5g**, **5j**, **5l**, and **5n** with phenyl substituents at the central nitrogen atom (R^2 = H) was likewise analyzed by TD-DFT calculations (Figure 12). With decreasing donor strength and increasing acceptor strength, the HOMO energy decreases. A similar effect is observed for the LUMO energy. The FMO show that, for all derivatives except **4b**, the HOMO is primarily localized on the TAA unit, while the LUMO is mainly distributed over the biaryl moiety, thereby inducing a CT from the TAA to the biaryl. In contrast, in **4b** the HOMO coefficient density is delocalized over the entire molecule, which, despite the altered dipole orientation, does not lead to a significantly different emission behavior.

The plot of $\Delta E(E_{HOMO}\text{-}E_{LUMO})$ against the substituent parameter σ_p^- results in excellent correlations ($r^2 = 0.967$ (**4b**, **4f**, **4k**, **4n**, and **4p**) and $r^2 = 0.954$ (**5c**, **5g**, **5j**, **5l**, and **5n**)) (see SI, chpt. 7.1, Figure S232 and S238). The negative correlation shows that $\Delta E(E_{HOMO}\text{-}E_{LUMO})$ decreases with diminishing donor strength, which should be accompanied by a bathochromic shift of the absorption band. Apparently, resonance effects of electron-withdrawing substituents directly influence the energy gap, since the LUMO is localized on the biaryl unit close to R^1, where donor groups act destabilizing and acceptor groups act stabilizing.

The Jabłoński diagrams likewise show that, in contrast to the consanguineous series **4h-l** and **5e-h** with variable R^2, the S_1 state energies reduce with decreasing donor strength of R^1 (Figure 13). The emission thus shifts bathochromically with diminishing donor character, which is consistent with the experimental results. In analogy to the plots of the experimental emission maxima, the calculated emission maxima also show the highest

TABLE 5 | UV/Vis absorption and emission maxima, absolute fluorescence quantum yields Φ_F and stokes shifts $\Delta\tilde{\nu}_S$ of *sym-m*-bTAA **4q** and *sym-o*-bTAA **5m** depending on solvent polarity.

	$\lambda_{max,abs}$, nm[a] (ε, $M^{-1}cm^{-1}$)		$\lambda_{max,\ em}$, nm[b] (Φ_F)[c]		$\Delta\tilde{\nu}_S$, cm^{-1}[d]		a, (Å)[e]	
Solvent	**4q**	**5m**	**4q**	**5m**	**4q**	**5m**	**4q**	**5m**
Cyclo-hexane	282 (42 200), 376 (sh, 2100),	272 (19 500), 304 (14 000), 380 (sh, 1600)	455 (0.70)	477 (0.18)	4600	5400	6.1	6.2
Toluene	287 (33 600), 380 (sh, 1900)	286 (18 700), 307 (16 600), 388 (sh, 1600)	487 (0.18)	501 (0.46)	5800	5800	5.9	6.1
THF	282 (35 800), 378 (sh, 1279)	271 (27 100), 305 (17 600), 389 (sh, 1900)	562 (0.03)	527 (0.17)	8700	6700	6.1	6.0
Ethyl acetate	283 (26 700), 376 (sh, 1400)	271 (29 200), 304 (20 000), 380 (sh, 2300)	560 (0.03)	525 (0.13)	10 800	7300	5.7	6.1
Dichloro-methane	281 (38 400), 379 (sh, 8700)	269 (27 500), 307 (19 000), 388 (sh, 2100)	562 (0.01)	546 (0.16)	8600	7500	6.1	6.3
DMF	280 (33 200), 378 (sh, 1800)	274 (25 300), 305 (16 700), 380 (sh, 10 000)	—	565 (0.06)	—	8600	5.7	6.0
DMSO	282 (38 300), 384 (sh, 1700)	273 (24 200), 309 (14 400), 385 (sh, 2000)	—	571 (0.04)	—	8500	5.7	6.0
Aceto-nitrile	278 (56 100), 379 (2000)	269 (24 400), 303 (16 400), 380 (sh, 2000)	—	563 (0.31)	—	8600	5.8	5.9
Ethanol	280 (12 100), 381 (sh, 1000)	271 (24 800), 305 (16 600), 385 (sh, 2100)	—	563 (0.03)	—	8200	5.8	6.0

[a]Recorded in different solvents, $T = 293$ K, $c = 10^{-5}$ M.
[b]Recorded in different solvents, $T = 293$ K, $c = 10^{-7}$ M.
[c]Absolute quantum yields recorded in different solvents, $T = 293$ K, $c = 10^{-7}$ M.
[d]$\Delta\tilde{\nu}_s = \frac{1}{\lambda_{max,abs}} - \frac{1}{\lambda_{max,em}}$.
[e]DFT calculations of the Onsager radius a (Gaussian 16, PBE1PBE/6-31+G** dipole, a_0(**4q**) = 5.9[f] or a_0(**5m**) = 6.3[f], volume) with different solvents, [f] Onsager radius a_0 of gas phase geometry (in Å).

correlation with the substituent parameter σ_p^- ($r^2 = 0.955$ (**4b**, **4f**, **4k**, **4n**, and **4p**) and $r^2 = 0.995$ (**5c**, **5g**, **5j**, **5l**, and **5n**)) (see SI, chpt. 7.1, Figure S233 and S239). In contrast, plots of the TD-DFT calculated Stokes shifts $\tilde{\nu}_{S,calcd}$ against the various Hammett parameters only correlate poorly, indicating that R^1 has only a minor influence on molecular relaxation and structural changes in the excited state.

The TD-DFT-based prediction derived here, with excellent correlation coefficients ($r^2 = 0.954$–0.998), demonstrates that rational molecular design based on the TD-DFT level of theory also constitutes an effective tool for the development of tailored *sym-m*/*o*-bTAA **4** and **5**.

2.6 | Emission Solvatochromism

For the isomers **4q** and **5m**, a pronounced emission solvatochromism can already be seen with the naked eye (Figure 14), where the emission color changes from blue (cyclohexane, **4q** and **5m**) to yellow (ethyl acetate, **4q**) or red (acetonitrile, **5m**). The emission solvatochromism was analyzed by absorption and emission spectroscopy in solvents of varying polarity to assess the dipolar character of the excited state (Table 5).

Normalization of all spectra was carried out with respect to the longest wavelength absorption, as this could be clearly determined experimentally for both isomers **4q** and **5m** in all solvents (Figure 15). While solvent polarity affects the positioning of the absorption shoulder only slightly within a narrow range from 376 to 389 nm, the emission spectra exhibit pronounced positive solvatochromism with bands between 455 and 571 nm. For **4q**, no emission could be detected in polar solvents. The emission of **5m** is slightly hypsochromically shifted in acetonitrile and ethanol compared to DMSO, presumably due to specific solvent effects such as hydrogen bonding, which already has a stronger influence on the dipole moment in the ground state.

The emission solvatochromism arises from a substantial dipole moment change $\Delta\mu$ of the fluorophore upon excitation and solvent dipole relaxation [55]. This change ($\Delta\mu$) was quantified using the Lippert–Mataga model, with the orientation polarizability Δf calculated from ε_r (relative permittivity) and n (optical refractive index) according to Equation (1).

$$\Delta f = \frac{\varepsilon_r - 1}{2\varepsilon_r + 1} - \frac{n^2 - 1}{2n^2 + 1} \quad (1)$$

The $\Delta\mu$ between the electronic ground and the vibrationally excited state was calculated with the Lippert–Mataga Equation (2),

$$\tilde{\nu}_a - \tilde{\nu}_f = \frac{2 \cdot \Delta f}{4 \cdot \pi \cdot \varepsilon_0 \cdot h \cdot c \cdot a^3} \cdot (\mu_E - \mu_G)^2 + \text{const.} \quad (2)$$

where $\tilde{\nu}_a$ and $\tilde{\nu}_f$ are the absorption and emission maxima (in m^{-1}), μ_E and μ_G the dipole moments in the excited and ground state (in Cm), ε_0 ($8.8542 \cdot 10^{-12}$ As V^{-1} m^{-1}) the vacuum permittivity constant, h ($6.6256 \cdot 10^{-34}$ Js) Planck's constant, and c ($2.9979 \cdot 10^8$ ms^{-1}) the speed of light. The Onsager radius a (in Å), approximating the molecular cavity in solution, was estimated from the DFT-optimized ground state structure of the gas phase (a_0(**4q**) = 5.9 Å and a_0(**5m**) = 6.3 Å) for each solvent (Table 5) [56–61]. Considering the solvent-specific Onsager radius a, the Lippert–Mataga plot of the Stokes shift $\Delta\tilde{\nu}_S$ against orientation polarizability

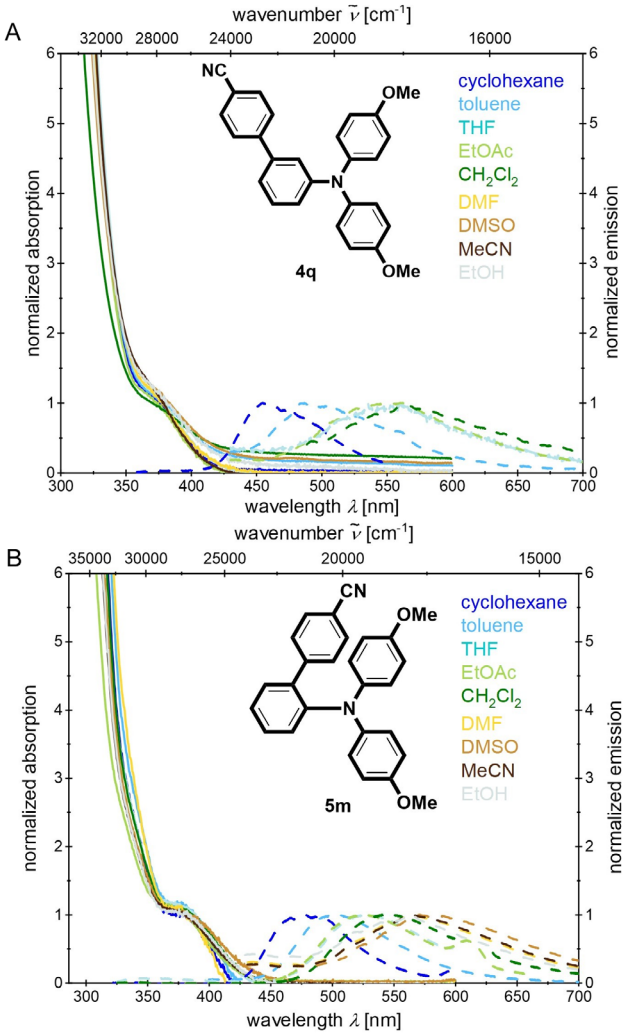

FIGURE 15 | Comparison of the UV/Vis absorption and emission spectra (absorption spectra recorded in nine solvents with different polarity, $T = 293$ K, $c = 10^5$ M (bold lines) and emission spectra recorded in nine solvents with different polarity, $T = 293$ K, $c = 10^7$ M (dashed lines)) of (**A**) *sym-m*-bTAA **4q** and (**B**) *sym-o*-bTAA **5m**.

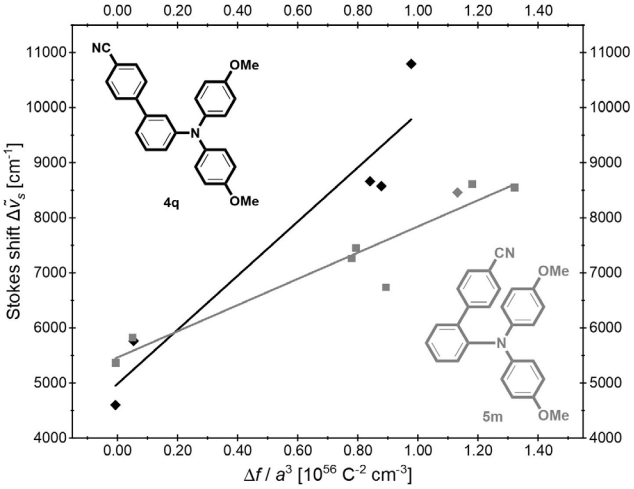

FIGURE 16 | Lippert plot for *sym-m*-bTAA **4q** ($\Delta\tilde{\nu}_S = 4.92 \cdot 10^{-53} \cdot \Delta f \cdot a^{-3} + 4980$ [cm^1], $r^2 = 0.914$) and *sym-o*-bTAA **5m** ($\Delta\tilde{\nu}_S = 2.38 \cdot 10^{-53} \cdot \Delta f \cdot a^{-3} + 5460$ [cm^1], $r^2 = 0.907$).

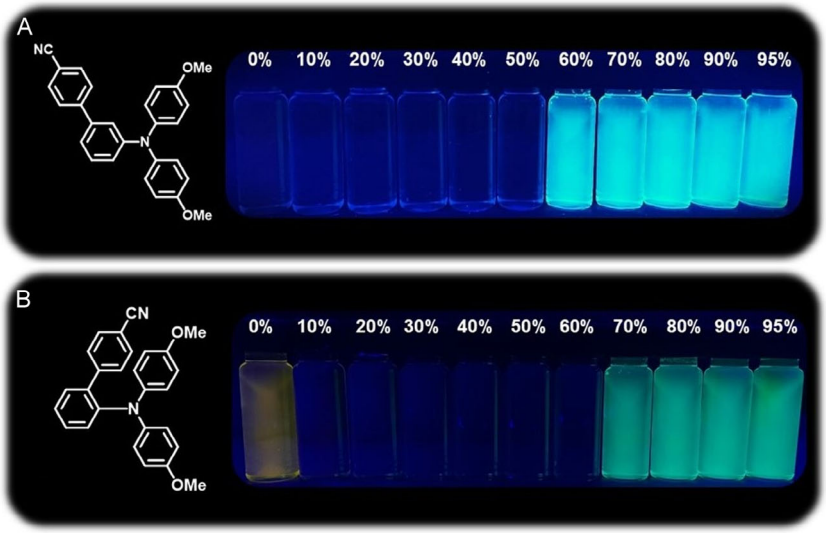

FIGURE 17 | Qualitative AIE study in different DMSO/water mixtures of (**A**) *sym-m*-bTAA **4q** and (**B**) *sym-o*-bTAA **5m** under irradiation with UV light ($\lambda_{exc} = 356$ nm, $T = 298$ K, $c = 10^{-5}$ M).

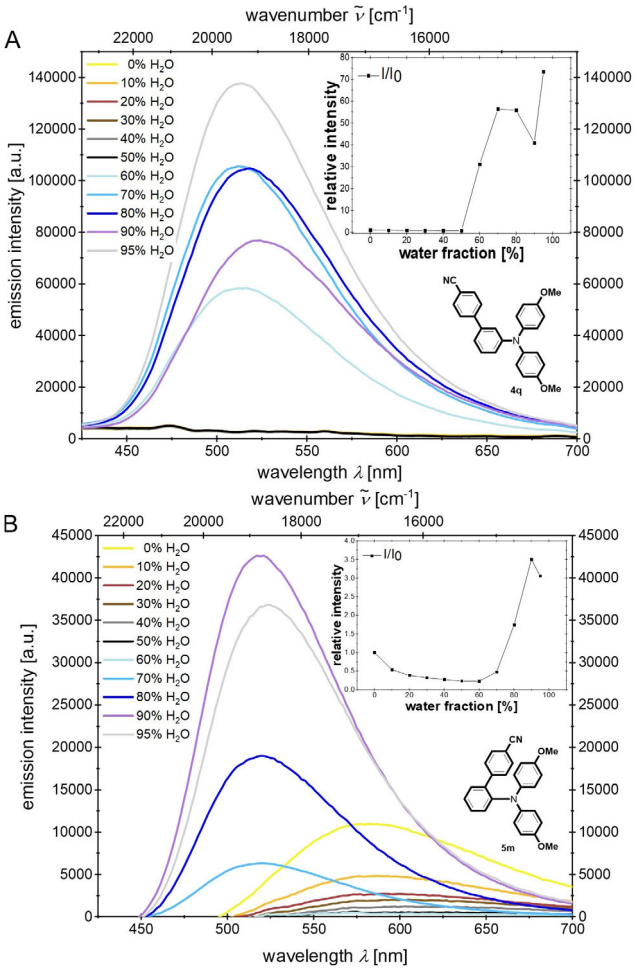

FIGURE 18 | Emission spectra of (**A**) *sym-m*-bTAA **4q** and (**B**) *sym-o*-bTAA **5m** in different DMSO/water mixtures ($T = 293$ K, $c = 10^{-7}$ M). The inset in the upper right depicts the change in emission intensity accompanied by the different water fractions.

Δf yields a $\Delta\mu$ of 21.0 D ($7.01 \cdot 10^{-29}$ Cm) for **4q** and 14.5 D ($4.88 \cdot 10^{-29}$ Cm) for **5m**. The linear correlations in Figure 16 indicate a dominant general solvent effect.

The $\Delta\mu$ of **5m** is significantly lower than that of *sym-p*-bTAA [39] and *sym-m*-bTAA **4q**, resulting in weaker emission solvatochromism for **5m** [62]. This is also reflected in the emission maxima because **5m** emits in DMSO at 571 nm, whereas **4q** shows no apparent emission there, but already in ethyl acetate it is markedly red-shifted to 560 nm compared to **5m** (525 nm). The *meta*-biaryl substitution of **4q** evidently leads to stronger spatial separation of HOMO and LUMO, while the *ortho*-biaryl substitution of **5m** promotes orbital proximity. For **4q**, the increased $\Delta\mu$ indicates a more pronounced CT character due to asymmetric charge separation. The previously discussed DFT calculations (vide supra) suggest that in *ortho*-isomers **5**, despite twisting, favorable proximity between the biaryl and triarylamine parts can persist, facilitating orbital overlap and coupling. The resulting enhanced delocalization of electron density across the entire π-system could plausibly explain the reduced CT character and lower $\Delta\mu$ of **5m**.

2.7 | Aggregation-Induced Emission

The AIE properties of isomers **4q** and **5m** were also examined in DMSO/water mixtures with water contents ranging from 0 to 95%. In pure DMSO, **4q** exhibits no detectable fluorescence, whereas **5m** displays weak yellow emission (Figure 17). Upon reaching a water content of ≈60% (**4q**) or 70% (**5m**), blue emission lights up, attributable to the induced formation of aggregates. The relative emission intensity of dyes **4q** and **5m** shows a clear dependence on the water fraction (Figure 18).

For dye **4q**, no emission is detectable in pure DMSO up to a water fraction of 60%. Above 60%, a maximum appears at 514 nm with sharply increasing intensity, achieving 75 times the initial intensity at 95% water fraction. The emission maxima vary between 512 and

524 nm, and the fluorescence quantum yield reaches up to $\Phi_F = 0.02$ (80% water fraction). In contrast, **5m** already shows a maximum at 571 nm ($\Phi_F = 0.04$) in pure DMSO, whose intensity decreases up to 60% water fraction. Above 70% water fraction, a hypsochromically shifted aggregation maximum appears at 519 nm, which reaches 3.5 times the initial intensity at a water content of 90% (517 nm). The emission maxima vary between 517 and 523 nm, and the fluorescence quantum yield reaches up to $\Phi_F = 0.10$ (80% water fraction). Time-dependent measurements further illustrate the limited stability of the aggregates (see SI, chpt. 13, Figure S14). After 2 days, the intensity remains at about 75%, but after 10 days only around 25% (**4q**) or 23% (**5m**), with no regeneration possible by ultrasound treatment.

3 | Conclusion

Sequential (*pseudo*-)four-component syntheses employing Suzuki coupling Buchwald–Hartwig amination sequences offer a modular strategy for accessing novel (*un*)*sym*-*m*- and -*o*-bTAA, achieving yields as high as 97%. Oxidation potentials correlate with the electronic nature of the substituents R^1 and R^2, with R^2 exerting the stronger influence. This dependence can be semiquantitatively determined by linear correlation with σ_p and exploited for the rationally fine-tuning oxidation potentials. In addition to reversible redox processes, derivatives bearing H or F substituents in R^2 exhibit irreversible processes, indicative of dimerization. Moreover, the photonic properties, investigated by absorption and emission spectroscopy, and transitions can be reliably assigned by TD-DFT calculations. The absorption and emission maxima are adjustable through substituents R^1 and R^2, and the dependence of the emission maxima can be illustrated by linear correlation with σ_p^- (R^1) and σ_p^+ (R^2). Significant positive emission solvatochromism is observed and the Lippert–Mataga analysis shows the largest dipole moment change $\Delta\mu$ for the *meta*-isomer, consistent with a pronounced CT character. In addition, AIE was observed in DMSO/water mixtures, with up to a 75-fold increase in intensity for the *meta*-isomer. The gained insights provide new opportunities for the rational design of novel, finely tunable bTAA emitters. Ongoing studies are focused on expanding the synthetic route by incorporating further coupling reactions and the homocoupling of *m*-, *o*-, and *p*-bTAAs to the corresponding dimers.

4 | General Methods

4.1 | MCR of *Sym*-*m*-bTAA 4g (Typical Procedure I)

Under nitrogen in a Schlenk tube with magnetic stir bar 3-iodoaniline (**1a**) (110 mg, 0.500 mmol, 1.00 equiv), (4-methoxyphenyl) boronic acid **2b** (84 mg, 0.550 mmol, 1.10 equivs), bis(dibenzylideneacetone)palladium(0) (14.0 mg, 25.0 µmol, 5.00 mol%), tri-*tert*-butylphosphane tetrafluoroborate (15.0 mg, 50.0 µmol, 10.0 mol%), and cesium carbonate (570 mg, 1.75 mmol, 3.50 equivs) were dissolved in dry 1,4-dioxane (3.5 mL). Then, the reaction mixture was stirred at 120°C (oil bath temperature) for 1 h. After cooling to room temperature, 1-bromo-4-fluorobenzene **3e** (219 mg, 1.25 mmol, 2.50 equivs) and sodium *tert*-butoxide (240 mg, 2.50 mmol, 5.00 equivs) were successively added. Then, the reaction mixture was stirred at 120°C (oil bath temperature) for 15 h. After cooling to room temperature, deionized water (50 mL) and dichloromethane (50 mL) were added. The aqueous phase was extracted with dichloromethane (3 × 10 mL). The combined organic phases were dried with anhydrous magnesium sulfate and the solvents were removed in vacuo. The residue was purified by flash chromatography on silica gel (*n*-hexane/ethyl acetate 15:1) and by recrystallization from *n*-hexane to give compound **4g** (156 mg, 0.402 mmol, 81%) as colorless crystals. Mp 117°C. R_f 0.60 (*n*-hexane/ethyl acetate 10:1). ^{1}H NMR (300 MHz, acetone-d_6) δ 3.81 (s, 3 H), 6.91 (ddd, $^3J = 7.9$ Hz, $^4J = 2.3$ Hz, 1.2 Hz, 1 H), 6.94–7.00 (m, 2 H), 7.05–7.17 (m, 8 H), 7.19–7.27 (m, 2 H), 7.32 (t, $^3J = 7.7$ Hz, 1 H), 7.42–7.49 (m, 2 H). ^{13}C NMR (150 MHz, acetone-d_6) δ 55.6 (CH_3), 115.1 (CH), 117.0 (d, CH, $^2J = 22.8$ Hz), 121.5 (CH), 121.6 (CH), 121.9 (CH), 127.1 (d, CH, $^3J = 8.1$ Hz), 128.7 (CH), 130.7 (CH), 133.8 (C_{quat}), 142.9 (C_{quat}), 145.1 (d, C_{quat}, $^4J = 2.8$ Hz), 149.5 (C_{quat}), 159.8 (d, C_{quat}, $^1J = 241.0$ Hz), 160.5 (C_{quat}). EI MS (70 eV, m/z (%)) 388 (23), 387 ([M]$^+$, 100), 279 ([$C_{18}H_{11}F_4N$]$^+$, 13), 57 ([C_3H_2F]$^+$, 15), 56 ([C_3H_4O]$^+$, 17). IR ($\tilde{\nu}$ [cm^{-1}]) 1580 (w), 1568 (w), 1501 (s), 1479 (s), 1441 (m), 1418 (w), 1404 (w), 1317 (m), 1277 (m), 1265 (w), 1240 (s), 1211 (s), 1177 (s), 1153 (m), 1113 (w), 1092 (m), 1051 (w), 1024 (m), 1011 (w), 995 (w), 949 (w), 916 (w), 885 (w), 831 (s), 822 (m), 800 (m), 783 (s), 741 (m), 725 (w), 700 (s), 664 (w), 644 (w), 625 (m). Anal. calcd. for $C_{25}H_{19}F_2NO$ [387.4] C 77.50, H 4.94, N 3.62; Found C 77.34, H 4.96, N 3.34.

4.2 | MCR of *Sym*-*o*-bTAA 5d (Typical Procedure II)

Under nitrogen in a Schlenk tube with magnetic stir bar 2-iodoaniline (**1b**) (110 mg, 0.500 mmol, 1.00 equiv), (4-methoxyphenyl) boronic acid **2b** (84 mg, 0.550 mmol, 1.10 equivs), bis(dibenzylideneacetone)palladium(0) (14.0 mg, 25.0 µmol, 5.00 mol%), tri-*tert*-butylphosphane tetrafluoroborate (15.0 mg, 50.0 µmol, 10.0 mol%), and cesium carbonate (570 mg, 1.75 mmol, 3.50 equiv) were dissolved in dry 1,4-dioxane (3.5 mL). Then, the reaction mixture was stirred at 120°C (oil bath temperature) for 1 h. After cooling to room temperature, 1-bromo-4-fluorobenzene **3e** (350 mg, 2.00 mmol, 4.00 equivs) and sodium *tert*-butoxide (240 mg, 2.50 mmol, 5.00 equivs) were successively added. Then, the reaction mixture was stirred at 120°C (oil bath temperature) for 30 h. After cooling to room temperature, deionized water (50 mL) and dichloromethane (50 mL) were added. The aqueous phase was extracted with dichloromethane (3 × 10 mL). The combined organic phases were dried with anhydrous magnesium sulfate and the solvents were removed in vacuo. The residue was purified by flash chromatography on silica gel (*n*-hexane/ethyl acetate 15:1) and by recrystallization from *n*-hexane to give compound **5d** (186 mg, 0.480 mmol, 96%) as colorless crystals. Mp 151°C. R_f 0.66 (*n*-hexane/ethyl acetate 10:1). ^{1}H NMR (600 MHz, acetone-d_6) δ 3.72 (s, 3 H), 6.73–6.76 (m, 2 H), 6.78–6.82 (m, 4 H), 6.86–6.91 (m, 4 H), 7.13–7.17 (m, 2 H), 7.23 (dd, $^3J = 7.9$ Hz, $^4J = 1.3$ Hz, 1 H), 7.31 (ddd, $^3J = 7.7$ Hz, 7.0 Hz, $^4J = 1.3$ Hz, 1 H), 7.34 (dd, $^3J = 7.7$ Hz, $^4J = 1.9$ Hz, 1 H), 7.38 (ddd, $^3J = 7.9$ Hz, 7.0 Hz, ^4J = 1.9 Hz, 1 H). ^{13}C NMR (150 MHz, acetone-d_6) δ 55.5 (CH_3), 114.3 (CH), 116.2 (d, CH, $^2J = 22.9$ Hz), 124.2 (d, CH, $^3J = 8.1$ Hz), 126.9 (CH), 129.5 (CH), 129.8 (CH), 130.4 (CH), 132.7 (CH), 132.9 (C_{quat}), 140.7 (C_{quat}), 145.1 (d, C_{quat}, $^4J = 2.6$ Hz), 145.7 (C_{quat}), 158.8 (d, C_{quat}, ^1J = 297.6 Hz), 159.4 (C_{quat}). EI MS (70 eV, m/z (%)) 388 (23), 387 ([M]$^+$, 100), 279 ([$C_{18}H_{11}F_2$]$^+$, 12), 248 (12), 203 ([$C_{12}H_7F_2N$]$^+$, 12), 139 (20), 96 ([C_6H_7O]$^+$, 14), 95 ([C_6H_7O]$^+$, 21), 75 (19). IR ($\tilde{\nu}$ [cm^{-1}]) 1604 (w), 1494 (s), 1477 (m), 1454 (w), 1443 (m), 1408 (w), 1312 (m),

1288 (w), 1275 (m), 1275 (m), 1248 (m), 1227 (m), 1207 (m), 1177 (s), 1155 (m), 1099 (w), 1096 (w), 1045 (w), 1034 (m), 1015 (w), 1001 (w), 949 (w), 922 (w), 870 (w), 826 (s), 799 (s), 754 (s), 719 (m), 698 (w), 683 (w), 656 (w). Anal. calcd. for $C_{25}H_{19}F_2NO$ [387.4] C 77.50, H 4.94, N 3.62; Found C 77.74, H 4.91, N 3.51.

4.3 | MCR of *Unsym-m*-bTAA 7a (Typical Procedure III)

Under nitrogen in a Schlenk tube with magnetic stir bar 3-iodoaniline (**1a**) (110 mg, 0.500 mmol, 1.00 equiv), (4-methoxyphenyl)boronic acid **2b** (84 mg, 0.550 mmol, 1.10 equivs), bis(dibenzylideneacetone)palladium(0) (14.0 mg, 25.0μmol, 5.00 mol%), tri-*tert*-butylphosphane tetrafluoroborate (14.0 mg, 50.0 µmol, 10.0 mol%), and cesium carbonate (570 mg, 1.75 mmol, 3.50 equiv) were dissolved in dry 1,4-dioxane (3.5 mL). Then, the reaction mixture was stirred at 120°C (oil bath temperature) for 1 h. After cooling to room temperature, 1-bromo-4-fluorobenzene **3e** (88 mg, 0.500 mmol, 1.00 equiv) and sodium *tert*-butoxide (96.0 mg, 1.00 mmol, 2.00 equivs) were successively added. Then, the reaction mixture was stirred at 120°C (oil bath temperature) for 15 h. After cooling to room temperature, bromobenzene **3d** (118 mg, 0.750 mmol, 1.50 equivs) and again sodium *tert*-butoxide (144 mg, 1.50 mmol, 3.00 equivs) were successively added. Then, the reaction mixture was stirred at 120°C (oil bath temperature) for 15 h. After cooling to room temperature, deionized water (50 mL) and dichloromethane (50 mL) were added. The aqueous phase was extracted with dichloromethane (3 × 10 mL). The combined organic phases were dried with anhydrous magnesium sulfate and the solvents were removed in vacuo. The residue was purified by flash chromatography on silica gel (*n*-hexane/ethyl acetate 15:1) and by recrystallization from *n*-hexane to give compound **7a** (126 mg, 0.341 mmol, 68%) as colorless crystals. Mp 106°C. R_f 0.55 (*n*-hexane/ethyl acetate 10:1). ^{1}H NMR (600 MHz, acetone-d_6) δ 3.81 (s, 3 H), 6.87–7.00 (m, 3 H), 7.01–7.17 (m, 7 H), 7.20–7.37 (m, 5 H), 7.40–7.51 (m, 2 H). ^{13}C NMR (150 MHz, acetone-d_6) δ 55.6 (CH_3), 115.1 (CH), 117.0 (d, CH, ^2J = 22.6 Hz), 121.7 (CH), 122.3 (CH), 122.5 (CH), 123.7 (CH), 124.5 (CH), 127.7 (d, CH, ^3J = 8.3 Hz), 128.7 (CH), 130.3 (CH), 130.7 (CH), 133.8 (C_{quat}), 142.5 (C_{quat}), 145.0 (d, C_{quat}, ^4J = 2.8 Hz), 148.8 (C_{quat}), 149.4 (C_{quat}), 159.8 (d, C_{quat}, ^1J = 243.8 Hz), 160.5 (C_{quat}). EI MS (70 eV, m/z (%)) 370 (23), 369 ([M]$^+$, 100), 351 ([$C_{25}H_{21}NO$]$^+$, 14), 261 ([$C_{18}H_{12}FN$]$^+$, 9). IR ($\tilde{\nu}$ [cm^{-1}]) 1605 (m), 1589 (m), 1570 (m), 1516 (m), 1491 (s), 1477 (s), 1456 (m), 1443 (m), 1400 (w), 1323 (m), 1314 (m), 1285 (m), 1242 (s), 1209 (s), 1180 (s), 1146 (w), 1109 (w), 1089 (m), 1047 (w), 1022 (m), 1009 (w), 991 (w), 980 (w), 930 (w), 880 (w), 845 (m), 827 (s), 816 (s), 791 (m), 741 (s), 739 (m), 718 (m), 694 (s), 644 (w), 629 (m), 606 (s). Anal. calcd. for $C_{25}H_{20}FNO$ [369.4] C 81.28, H 5.46, N 3.79; Found C 81.48, H 5.59, N 3.66.

4.4 | MCR of *Unsym-o*-bTAA 8x (Typical Procedure IV)

Under nitrogen in a Schlenk tube with magnetic stir bar 2-iodoaniline (**1b**) (110 mg, 0.500 mmol, 1.00 equiv), (4-methoxyphenyl) boronic acid **2b** (84 mg, 0.550 mmol, 1.10 equivs), bis(dibenzylideneacetone)palladium(0) (14.0 mg, 25.0 µmol, 5.00 mol%), tri-*tert*-butylphosphane tetrafluoroborate (15.0 mg, 50.0 µmol, 10.0 mol%), and cesium carbonate (570 mg, 1.75 mmol, 3.50 equivs) were dissolved in dry 1,4-dioxane (3.5 mL). Then, the reaction mixture was stirred at 120°C (oil bath temperature) for 1 h. After cooling to room temperature, 1-bromo-4-fluorobenzene **3e** (88 mg, 0.500 mmol, 1.00 equiv) and sodium *tert*-butoxide (96.0 mg, 1.00 mmol, 2.00 equivs) were successively added. Then, the reaction mixture was stirred at 120°C (oil bath temperature) for 15 h. After cooling to room temperature, bromobenzene **3d** (236 mg, 1.50 mmol, 3.00 equivs) and again sodium *tert*-butoxide (144 mg, 1.50 mmol, 3.00 equivs) were successively added. Then, the reaction mixture was stirred at 120°C (oil bath temperature) for 15 h. After cooling to room temperature, deionized water (50 mL) and dichloromethane (50 mL) were added. The aqueous phase was extracted with dichloromethane (3 x 10 mL). The combined organic phases were dried with anhydrous magnesium sulfate and the solvents were removed in vacuo. The residue was purified by flash chromatography on silica gel (*n*-hexane/ethyl acetate 10:1) and by recrystallization from *n*-hexane to give compound **8a** (179 mg, 0.485 mmol, 97%) as colorless crystals. Mp 150°C. R_f 0.59 (*n*-hexane/ethyl acetate 10:1). ^{1}H NMR (600 MHz, acetone-d_6) δ 3.72 (s, 3 H), 6.72–6.75 (m, 2 H), 6.76–6.80 (m, 2 H), 6.81–6.87 (m, 5 H), 7.11–7.14 (m, 2 H), 7.14–7.17 (m, 2 H), 7.25 (dd, ^3J = 7.9 Hz, ^4J = 1.3 Hz, 1 H), 7.31 (ddd, ^3J = 7.8 Hz, 7.0 Hz, ^4J = 2.0 Hz, 1 H), 7.35 (dd, ^3J = 7.7 Hz, ^4J = 1.9 Hz, 1 H), 7.39 (ddd, ^3J = 7.8 Hz, 7.0 Hz, ^4J = 1.9 Hz, 1 H). ^{13}C NMR (150 MHz, acetone-d_6) δ 55.5 (CH_3), 114.2 (CH), 116.2 (d, CH, ^2J = 22.6 Hz), 121.9 (CH), 121.6 (CH), 125.2 (d, CH, ^3J = 8.1 Hz), 127.0 (CH), 129.5 (CH), 129.8 (CH), 130.2 (CH), 130.4 (CH), 132.7 (CH), 132.9 (C_{quat}), 141.0 (C_{quat}), 144.5 (d, C_{quat}, ^4J = 2.6 Hz), 145.6 (C_{quat}), 149.0 (C_{quat}), 158.8 (d, C_{quat}, ^1J = 239.5 Hz), 159.8 (C_{quat}). EI MS (70 eV, m/z (%)) 370 (24), 369 ([M]$^+$, 100), 261 ([$C_{18}H_{12}FN$]$^+$, 12). IR ($\tilde{\nu}$ [cm^{-1}]) 1611 (w), 1585 (w), 1516 (w), 1501 (m), 1491 (m), 1480 (m), 1456 (w), 1441 (w), 1408 (w), 1393 (w), 1310 (m), 1290 (w), 1273 (m), 1244 (m), 1209 (w), 1179 (m), 1152 (m), 1096 (w), 1080 (w), 1045 (w), 1032 (m), 1016 (w), 995 (w), 978 (w), 918 (w), 883 (w), 870 (w), 833 (m), 812 (m), 800 (m), 750 (s), 721 (m), 694 (m), 615 (m). Anal. calcd. for $C_{25}H_{19}F_2NO$ [387.4] C 81.28, H 5.46, N 3.79; Found C 81.36, H 5.50, N 3.72.

Acknowledgments

The authors are grateful to the DFG (Deutsche Forschungsgemeinschaft) (Mu 1088/9-1) and the Fonds der Chemischen Industrie for financial support. We also thank the CeMSA@HHU (Center for Molecular and Structural Analytics @ Heinrich Heine University) for recording the mass spectrometric and the NMR spectroscopic data.

Open Access funding enabled and organized by Projekt DEAL.

Funding

This study was supported by Deutsche Forschungsgemeinschaft (grant Mu 1088/9-1), Fonds der Chemischen Industrie.

Conflicts of Interest

The authors declare no conflicts of interest.

Data Availability Statement

The data that support the findings of this study are available in the SI of this article.

References

1. H. Zollinger, *Color Chemistry: Syntheses, Properties, and Applications of Organic Dyes and Pigments* (Wiley-VCH, 2003).

2. W. D. Callister and D. G. Rethwisch, *Materialwissenschaften Und Werkstofftechnik* (Wiley, 2020).

3. L. P. Hammett, "Some Relations between Reaction Rates and Equilibrium Constants," *Chemical Reviews* 17 (1935): 125–136.

4. L. P. Hammett, "Linear Free Energy Relationships in Rate and Equilibrium Phenomena," *Journal of the Chemical Society, Faraday Transactions* 34 (1938): 156–165.

5. L. P. Hammett, "The Effect of Structure upon the Reactions of Organic Compounds. Benzene Derivatives," *Journal of the American Chemical Society* 59 (1937): 96–103.

6. T. J. J. Müller, *Functional Organic Materials: Syntheses, Strategies and Applications*, vol. 1, ed. Müller T. J. J., andBunz U. H. F., (Wiley-VCH, 2006), 179–223.

7. R. L. Carroll and C. B. Gorman, "The Genesis of Molecular Electronics," *Angewandte Chemie International Edition* 41 (2002): 4378–4400.

8. J. M. Tour, "Molecular Electronics. Synthesis and Testing of Components," *Accounts of Chemical Research* 33 (2000): 791–804.

9. O. Brügner, T. Reichenbach, M. Sommer, and M. Walter, "Substituent Correlations Characterized by Hammett Constants in the Spiropyran-Merocyanine Transition," *Journal of Physical Chemistry. A* 121 (2017): 2683–2687.

10. G. Maruccio, R. Cingolani, and R. Rinaldi, "Projecting the Nanoworld: Concepts, Results and Perspectives of Molecular Electronics," *Journal of Materials Chemistry* 14 (2004): 542–554.

11. J. Luo, Z. Xie, J. W. Y. Lam, et al., "Aggregation-Induced Emission of 1-Methyl-1,2,3,4,5-Pentaphenylsilole," *Chemical Communications* 2001): 1740–1741.

12. Y. Hong, J. W. Y. Lam, and B. Z. Tang, "Aggregation-Induced Emission: Phenomenon, Mechanism and Applications," *Chemical Communications* (2009): 4332–4353.

13. Y. Hong, J. W. Y. Lam, and B. Z. Tang, "Aggregation-Induced Emission," *Chemical Society Reviews* 40 (2011): 5361–5388.

14. J. Yang, Z. Chi, W. Zhu, B. Z. Tang, and Z. Li, "Aggregation-Induced Emission: A Coming-of-Age Ceremony at the Age of Eighteen," *Science China. Chemistry* 62 (2019): 1090–1098.

15. Z. Zhao, H. Zhang, J. W. Y. Lam, and B. Z. Tang, "Aggregation-Induced Emission: New Vistas at the Aggregate Level," *Angewandte Chemie International Edition* 59 (2020): 9888–9907.

16. J. Mei, N. L. C. Leung, R. T. K. Kwok, J. W. Y. Lam, and B. Z. Tang, "Aggregation-Induced Emission: Together We Shine, United We Soar!," *Chemical Reviews* 115 (2015): 11718–11940.

17. K. Kokado and K. Sada, "Consideration of Molecular Structure in the Excited State to Design New Luminogens with Aggregation-Induced Emission," *Angewandte Chemie International Edition* 58 (2019): 8632–8639.

18. G. A. Sommer, L. N. Mataranga-Popa, R. Czerwieniec, et al., "Design of Conformationally Distorted Donor-Acceptor Dyads Showing Efficient Thermally Activated Delayed Fluorescence," *The Journal of Physical Chemistry Letters* 9 (2018): 3692–3697.

19. W. Xu, M. M. S. Lee, Z. Zhang, et al., "Facile Synthesis of AIEgens with Wide Color Tunability for Cellular Imaging and Therapy," *Chemical Science* 10 (2019): 3494–3501.

20. J. Wang, K. Liu, L. Ma, and X. Zhan, "Triarylamine: Versatile Platform for Organic, Dye-Sensitized, and Perovskite Solar Cells," *Chemical Reviews* 116 (2016): 14675–14725.

21. G. Li, W. Dai, Y. Lei, et al., *Recent Advances in Organic Room Temperature Phosphorescence of Triphenylamine-Based Doping Systems" ChemPhotoChem* 7 (2022):, e202200198.

22. P. Blanchard, C. Malacrida, C. Cabanetos, J. Roncali, and S. Ludwigs, "Triphenylamine and Some of Its Derivatives as Versatile Building Blocks for Organic Electronic Applications," *Polymer International* 68 (2019): 589–606.

23. O. Yurchenko, D. Freytag, L. zur Borg, R. Zentel, J. Heinze, and S. Ludwigs, "Electrochemically Induced Reversible and Irreversible Coupling of Triarylamines," *Journal of Physical Chemistry. B* 116 (2012): 30–39.

24. Z. Li, Z. R. Li, and H. Meng, *Organic Light-Emitting Materials and Devices* (CRC Press, 2006).

25. L. Calió, S. Kazim, M. Grätzel, and S. Ahmad, "Hole-Transport Materials for Perovskite Solar Cells," *Angewandte Chemie International Edition* 55 (2016): 14522–14545.

26. K. P. Carter, A. M. Young, and A. E. Palmer, "Fluorescent Sensors for Measuring Metal Ions in Living Systems," *Chemical Reviews* 114 (2014): 4564–4601.

27. S. W. Thomas, G. D. Joly, and T. M. Swager, "Chemical Sensors Based on Amplifying Fluorescent Conjugated Polymers," *Chemical Reviews* 107 (2007): 1339–1386.

28. I. Ugi, B. Werner, and A. Dömling, "The Chemistry of Isocyanides, Their Multicomponent Reactions and Their Libraries," *Molecules* 8 (2003): 53–66.

29. A. Dömling and I. Ugi, "Multicomponent Reactions with Isocyanides," *Angewandte Chemie International Edition* 39 (2000): 3168–3210.

30. G. H. Posner, "Multicomponent One-Pot Annulations forming 3 to 6 Bonds," *Chemical Reviews* 86 (1986): 831–844.

31. T. Lessing and T. J. J. Müller, "Sequentially Palladium-Catalyzed Processes in One-Pot Syntheses of Heterocycles," *Applied Sciences*5 (2015): 1803–1836.

32. T. J. J. Müller, *Sequentially Palladium-Catalyzed Processes*, vol. 19, ed. T. J. J. Müller, (Springer, 2006), 149–205,

33. M. M. Kornet and T. J. J. Müller, "Recent Advances in Sequentially Pd-Catalyzed One-Pot Syntheses of Heterocycles," *Molecules* 29 (2024): 5265.

34. A. de Meijere and F. Diederich, *Metal-Catalyzed Cross-Coupling Reactions* (Wiley-VCH Verlag, 2004).

35. M. Beller and C. Bolm, *Transition Metals of Organic Synthesis: Building Blocks and Fine Chemicals* (WILEY-VCH, 2004).

36. G. Poli, G. Giambastiani, and A. Heumann, "Palladium in Organic Synthesis: Fundamental Transformations and Domino Processes," *Tetrahedron* 56 (2000): 5959–5989.

37. L. Mayer, R. Kohlbecher, and T. J. J. Müller, "Concatenating Suzuki Arylation and Buchwald–Hartwig Amination by A Sequentially Pd-Catalyzed One-Pot Process—Consecutive Three-Component Synthesis of C, N-Diarylated Heterocycles," *Chemistry A European Journal* 26 (2020): 15130–15134.

38. L. Mayer and T. J. J. Müller, "3,10-Diaryl Phenothiazines - One-Pot Synthesis and Conformational Tuning of Ground and Excited State Electronics," *European Journal of Organic Chemistry* 2021 (2021): 3516–3527.

39. R. Kohlbecher and T. J. J. Müller, "A Rational Design of Electrochemically and Photophysically Tunable Triarylamine Luminophores by Consecutive (Pseudo-)Four-Component Syntheses," *Chemistry A European Journal* 30 (2024): e202304119.

40. Y. Sunesson, E. Lime, S. O. Nilsson Lill, R. E. Meadows, and P.-O. Norrby, "Role of the Base in Buchwald-Hartwig Amination," *Journal of Organic Chemistry* 79 (2014): 11961–11969.

41. Y. Kanazawa, T. Yokota, H. Ogasa, et al., "Chemoselective Amination of Bromoiodobenzenes with Diarylamines by Palladium/Xantphos or Ligand-Free Copper Catalysts," *Tetrahedron* 71 (2015): 1395–1402.

42. Deposition numbers 2506109 (for 5c), 2506110 (for 5g), 2506111 (for 5m), and 2506112 (for 5n) contain the supplementary crystallographic data for this paper. These data are provided free of charge by the joint Cambridge Crystallographic Data Centre and Fachinformationszentrum Karlsruhe Access Structures service.,

43. A. R. Mallia, R. Ramakrishnan, M. A. Niyas, and M. Hariharan, "Crystalline Triphenylamine Substituted Arenes: Solid State Packing and Luminescence Properties," *CrystEngComm* 19 (2017): 817–825.

44. P. Cias, C. Slugovc, and G. Gescheidt, "Hole Transport in Triphenylamine Based OLED Devices: From Theoretical Modeling to Properties Prediction," *Journal of Physical Chemistry. A* 115 (2011): 14519–14525.

45. V. V. Pavlishchuk and A. W. Addison, "Conversion Constants for Redox Potentials Measured versus Different Reference Electrodes in Acetonitrile Solutions at 25°C," *Inorganica Chimica Acta*298 (2000): 97–102.

46. V. Kertesz and G. J. Van Berkel, "Monitoring Ionic Adducts to Elucidate Reaction Mechanisms: Reduction of Tetracyanoquinodimethane and Oxidation of Triphenylamine Investigated Using on-Line Electrochemistry/Electrospray Mass Spectrometry," *Journal of Solid State Electrochemistry : Current Research and Development in Science and Technology* 9 (2005): 390–397.

47. C. Hansch, A. Leo, and R. W. Taft, "A Survey of Hammett Substituent Constants and Resonance and Field Parameters," *Chemical Reviews* 91 (1991): 165–195.

48. R. Katoh, K. Suzuki, A. Furube, M. Kotani, and K. Tokumaru, "Fluorescence Quantum Yield of Aromatic Hydrocarbon Crystals," *Journal of Physical Chemistry C* 113 (2009): 2961–2965.

49. M. J. Frisch, G. W. Trucks, H. B. Schlegel, et al., "Gaussian 16, Revision-A.03".

50. J. P. Perdew, K. Burke, and M. Ernzerhof, "Generalized Gradient Approximation Made Simple," *Physical Review Letters* 77 (1996): 3865.

51. C. Adamo and V. Barone, "Toward Reliable Density Functional Methods without Adjustable Parameters: The PBE0 Model," *Journal of Chemical Physics* 110 (1999): 6158–6170.

52. R. Krishnan, J. S. Binkley, R. Seeger, and J. A. Pople, "Self-Consistent Molecular Orbital Methods. XX. A Basis Set for Correlated Wave Functions," *Journal of Chemical Physics* 72 (1980): 650–654.

53. G. Scalmani and M. J. Frisch, "Continuous Surface Charge Polarizable Continuum Models of Solvation.I. General Formalism," *Journal of Chemical Physics* 132 (2010): 114110.

54. H. Hopf and M. S. Sherburn, *Cross Conjugation: Modern Dendralene, Radialene and Fulvene Chemistry* (Wiley-VCH, 2016).

55. C. Reichardt and T. Welton, *Solvents and Solvent Effects in Organic Chemistry* (Wiley-VCH, 2010).

56. J. G. Kirkwood, "Theory of Solutions of Molecules Containing Widely Separated Charges with Special Application to Zwitterions," *Journal of Chemical Physics* 2 (1934): 351–361.

57. L. Onsager, "Electric Moments of Molecules in Liquids," *Journal of the American Chemical Society* 58 (1936): 1486–1493.

58. M. W. Wong, M. J. Frisch, and K. B. Wiberg, "Solvent Effects. 1. The Mediation of Electrostatic Effects by Solvents," *Journal of the American Chemical Society* 113 (1991): 4776–4782.

59. M. W. Wong, K. B. Wiberg, and M. Frisch, "Hartree–Fock Second Derivatives and Electric Field Properties in a Solvent Reaction Field: Theory and Application," *Journal of Chemical Physics* 95 (1991): 8991–8998.

60. M. W. Wong, K. B. Wiberg, and M. J. Frisch, "Solvent Effects. 2. Medium Effect on the Structure, Energy, Charge Density, and Vibrational Frequencies of Sulfamic Acid," *Journal of the American Chemical Society* 114 (1992): 523–529.

61. M. W. Wong, K. B. Wiberg, and M. J. Frisch, "Solvent Effects. 3. Tautomeric Equilibria of Formamide and 2-Pyridone in the Gas Phase and Solution: An Ab Initio SCRF Study," *Journal of the American Chemical Society* 114 (1992): 1645–1652.

62. J. R. Lakowicz, *Principles of Fluorescence Spectroscopy*, vol. 3, (Springer, 2006).

Supporting Information

Additional supporting information can be found online in the Supporting Information section. **Supporting Fig. S1:** ^{1}H NMR spectrum (acetone-d_6, 600 MHz, 298 K) of compound **4a**. **Supporting Fig. S2:** ^{13}C NMR spectrum (acetone-d_6, 150 MHz, 298 K) of compound **4a**. **Supporting Fig. S3:** ^{1}H NMR spectrum (acetone-d_6, 600 MHz, 298 K) of compound **4b**. **Supporting Fig. S4:** ^{13}C NMR spectrum (acetone-d_6, 150 MHz, 298 K) of compound **4b**. **Supporting Fig. S5:** ^{1}H NMR spectrum (acetone-d_6, 600 MHz, 298 K) of compound **4c**. **Supporting Fig. S6:** ^{13}C NMR spectrum (acetone-d_6, 150 MHz, 298 K) of compound **4c**. **Supporting Fig. S7:** ^{1}H NMR spectrum (acetone-d_6, 600 MHz, 298 K) of compound **4d**. **Supporting Fig. S8:** ^{13}C NMR spectrum (acetone-d_6, 150 MHz, 298 K) of compound **4d**. **Supporting Fig. S9:** ^{1}H NMR spectrum (acetone-d_6, 600 MHz, 298 K) of compound **4e**. **Supporting Fig. S10**. ^{13}C NMR spectrum (acetone-d_6, 150 MHz, 298 K) of compound **4e**. **Supporting Fig. S11:** ^{1}H NMR spectrum (acetone-d_6, 600 MHz, 298 K) of compound **4f**. **Supporting Fig. S12:** ^{13}C NMR spectrum (acetone-d_6, 150 MHz, 298 K) of compound **4f**. **Supporting Fig. S13:** ^{1}H NMR spectrum (acetone-d_6, 600 MHz, 298 K) of compound **4g**. **Supporting Fig. S14:** ^{13}C NMR spectrum (acetone-d_6, 150 MHz, 298 K) of compound **4g. Supporting Fig. S15:** ^{1}H NMR spectrum (acetone-d_6, 600 MHz, 298 K) of compound **4h. Supporting Fig. S16:** ^{13}C NMR spectrum (acetone-d_6, 150 MHz, 298 K) of compound **4h**. **Supporting Fig. S17:** ^{1}H NMR spectrum (acetone-d_6, 600 MHz, 298 K) of compound **4i**. **Supporting Fig. S18:** ^{13}C NMR spectrum (acetone-d_6, 150 MHz, 298 K) of compound **4i**. **Supporting Fig. S19:** ^{1}H NMR spectrum (acetone-d_6, 600 MHz, 298 K) of compound **4j**. **Supporting Fig. S20.** ^{13}C NMR spectrum (acetone-d_6, 150 MHz, 298 K) of compound **4j**. **Supporting Fig. S21:** ^{1}H NMR spectrum (acetone-d_6, 600 MHz, 298 K) of compound **4k. Supporting Fig. S22:** ^{13}C NMR spectrum (acetone-d_6, 150 MHz, 298 K) of compound **4k**. **Supporting Fig. S23:** ^{1}H NMR spectrum (acetone-d_6, 600 MHz, 298 K) of compound **4l**. **Supporting Fig. S24:** ^{13}C NMR spectrum (acetone-d_6, 150 MHz, 298 K) of compound **4l**. **Supporting Fig. S25:** ^{1}H NMR spectrum (acetone-d_6, 600 MHz, 298 K) of compound **4m**. **Supporting Fig. S26:** ^{13}C NMR spectrum (acetone-d_6, 150 MHz, 298 K) of compound **4m**. **Supporting Fig. S27:** ^{1}H NMR spectrum (acetone-d_6, 600 MHz, 298 K) of compound **4n**. **Supporting Fig. S28:** ^{13}C NMR spectrum (acetone-d_6, 150 MHz, 298 K) of compound **4n**. **Supporting Fig. S29:** ^{1}H NMR spectrum (acetone-d_6, 600 MHz, 298 K) of compound **4o**. **Supporting Fig. S30:** ^{13}C NMR spectrum (acetone-d_6, 150 MHz, 298 K) of compound **4o**. **Supporting Fig. S31:** ^{1}H NMR spectrum (acetone-d_6, 600 MHz, 298 K) of compound **4p**. **Supporting Fig. S32:** ^{13}C NMR spectrum (acetone-d_6, 150 MHz, 298 K) of compound **4p**. **Supporting Fig. S33:** ^{1}H NMR spectrum (acetone-d_6, 600 MHz, 298 K) of compound **4q**. **Supporting Fig. S34:** ^{13}C NMR spectrum (acetone-d_6, 150 MHz, 298 K) of compound **4q**. **Supporting Fig. S35:** ^{1}H NMR spectrum (acetone-d_6, 600 MHz, 298 K) of compound **4r**. **Supporting Fig. S36:** ^{13}C NMR spectrum (acetone-d_6, 150 MHz 298 K) of compound **4r**. **Supporting Fig. S37:** ^{1}H NMR spectrum (acetone-d_6, 600 MHz, 298 K) of compound **4s**. **Supporting Fig. S38:** ^{13}C NMR spectrum (acetone-d_6, 150 MHz, 298 K) of compound **4s**. **Supporting Fig. S39:** ^{1}H NMR spectrum (acetone-d_6, 600 MHz, 298 K) of compound **4t**. **Supporting Fig. S40:** ^{13}C NMR spectrum (acetone-d_6 150 MHz, 298 K) of compound **4t**. **Supporting Fig. S41:** ^{1}H NMR spectrum (acetone-d_6, 600 MHz, 298 K) of compound **5a**. **Supporting Fig. S42:** ^{13}C NMR spectrum (acetone-d_6, 150 MHz, 298 K) of compound **5a**. **Supporting Fig. S43:** ^{1}H NMR spectrum (acetone-d_6, 600 MHz, 298 K) of compound **5b**. **Supporting Fig. S44:** ^{13}C NMR spectrum (acetone-d_6, 150 MHz, 298 K) of compound **5b**. **Supporting Fig. S45:** ^{1}H NMR spectrum (acetone-d_6, 600 MHz, 298

K) of compound **5c**. **Supporting Fig. S46:** ^{13}C NMR spectrum (acetone-d_6, 150 MHz, 298 K) of compound **5c**. **Supporting Fig. S47:** ^{1}H NMR spectrum (acetone-d_6, 600 MHz 298 K) of compound **5d**. **Supporting Fig. S48:** ^{13}C NMR spectrum (acetone-d_6, 150 MHz, 298 K) of compound **5d**. **Supporting Fig. S49:** ^{1}H NMR spectrum (acetone-d_6, 600 MHz, 298 K) of compound **5e**. **Supporting Fig. S50:** ^{13}C NMR spectrum (acetone-d_6, 150 MHz, 298 K) of compound **5e**. **Supporting Fig. S51:** ^{1}H NMR spectrum (acetone-d_6, 600 MHz, 298 K) of compound **5f**. **Supporting Fig. S52:** ^{13}C NMR spectrum (acetone-d_6, 150 MHz, 298 K) of compound **5f**. **Supporting Fig. S53:** ^{1}H NMR spectrum (acetone-d_6, 600 MHz, 298 K) of compound **5g**. **Supporting Fig. S54:** ^{13}C NMR spectrum (acetone-d_6, 150 MHz, 298 K) of compound **5g**. **Supporting Fig. S55:** ^{1}H NMR spectrum (acetone-d_6, 600 MHz, 298 K) of compound **5h**. **Supporting Fig. S56:** ^{13}C NMR spectrum (acetone-d_6, 150 MHz, 298 K) of compound **5h**. **Supporting Fig. S57:** ^{1}H NMR spectrum (acetone-d_6 600 MHz, 298 K) of compound **5i**. **Supporting Fig. S58:** ^{13}C NMR spectrum (acetone-d_6, 150 MHz, 298 K) of compound **5i**. **Supporting Fig. S59:** ^{1}H NMR spectrum (acetone-d_6 600 MHz, 298 K) of compound **5j**. **Supporting Fig. S60:** ^{13}C NMR spectrum (acetone-d_6, 150 MHz, 298 K) of compound **5j**. **Supporting Fig. S61:** ^{1}H NMR spectrum (acetone-d_6, 600 MHz, 298 K) of compound **5k**. **Supporting Fig. S62**: ^{13}C NMR spectrum (acetone-d_6, 150 MHz, 298 K) of compound **5k**. **Supporting Fig. S63:** ^{1}H NMR spectrum (acetone-d_6, 600 MHz, 298 K) of compound **5l**. **Supporting Fig. S64:** ^{13}C NMR spectrum (acetone-d_6, 150 MHz, 298 K) of compound **5l**. **Supporting Fig. S65:** ^{1}H NMR spectrum (acetone-d_6, 600 MHz, 298 K) of compound **5m**. **Supporting Fig. S66:** ^{13}C NMR spectrum (acetone-d_6, 150 MHz, 298 K) of compound **5m**. **Supporting Fig. S67:** ^{1}H NMR spectrum (acetone-d_6, 600 MHz, 298 K) of compound **5n**. **Supporting Fig. S68:** ^{13}C NMR spectrum (acetone-d_6, 150 MHz, 298 K) of compound **5n**. **Supporting Fig. S69:** ^{1}H NMR spectrum (acetone-d_6, 600 MHz, 298 K) of compound **5o**. **Supporting Fig. S70:** ^{13}C NMR spectrum (acetone-d_6, 150 MHz, 298 K) of compound **5o**. **Supporting Fig. S71:** ^{1}H NMR spectrum (acetone-d_6, 600 MHz, 298 K) of compound **6a**. **Supporting Fig. S72:** ^{13}C NMR spectrum (acetone-d_6, 150 MHz, 298 K) of compound **6a**. **Supporting Fig. S73:** ^{1}H NMR spectrum (acetone-d_6, 600 MHz, 298 K) of compound **7a**. **Supporting Fig. S74:** ^{13}C NMR spectrum (acetone-d_6, 150 MHz, 298 K) of compound **7a**. **Supporting Fig. S75:** ^{1}H NMR spectrum (acetone-d_6, 600 MHz, 298 K) of compound **7b**. **Supporting Fig. S76:** ^{13}C NMR spectrum (acetone-d_6, 150 MHz, 298 K) of compound **7b**. **Supporting Fig. S77:** ^{1}H NMR spectrum (acetone-d_6, 600 MHz, 298 K) of compound **7c**. **Supporting Fig. S78:** ^{13}C NMR spectrum (acetone-d_6, 150 MHz, 298 K) of compound **7c**. **Supporting Fig. S79:** ^{1}H NMR spectrum (acetone-d_6, 600 MHz, 298 K) of compound **7d**. **Supporting Fig. S80:** ^{13}C NMR spectrum (acetone-d_6, 150 MHz, 298 K) of compound **7d**. **Supporting Fig. S81:** ^{1}H NMR spectrum (acetone-d_6, 600 MHz, 298 K) of compound **8a**. **Supporting Fig. S82:** ^{13}C NMR spectrum (acetone-d_6, 150 MHz, 298 K) of compound **8a**. **Supporting Fig. S83:** ^{1}H NMR spectrum (acetone-d_6, 600 MHz, 298 K) of compound **8b**. **Supporting Fig. S84:** ^{13}C NMR spectrum (acetone-d_6, 150 MHz, 298 K) of compound **8b**. **Supporting Fig. S85:** ^{1}H NMR spectrum (acetone-d_6, 600 MHz, 298 K) of compound **8c**. **Supporting Fig. S86:** ^{13}C NMR spectrum (acetone-d_6, 150 MHz, 298 K) of compound **8c**. **Supporting Fig. S87:** ^{1}H NMR spectrum (acetone-d_6, 600 MHz, 298 K) of compound **8d**. **Supporting Fig. S88:** ^{13}C NMR spectrum (acetone-d_6, 150 MHz, 298 K) of compound **8d**. **Supporting Fig. S89:** ^{1}H NMR spectrum (acetone-d_6, 600 MHz, 298 K) of compound **8e**. **Supporting Fig. S90:** ^{13}C NMR spectrum (acetone-d_6, 150 MHz, 298 K) of compound **8e**. **Supporting Fig. S91:** ^{1}H NMR spectrum (acetone-d_6, 600 MHz, 298 K) of compound **8f**. **Supporting Fig. S92:** ^{13}C NMR spectrum (acetone-d_6, 150 MHz, 298 K) of compound **8f**. **Supporting Fig. S93:** Cyclic voltammograms of compound **5j** recorded in dichloromethane (T = 293 K, ν = 100 mV/s, electrolyte: [nBu$_4$N][PF$_6$], Pt working electrode, Pt counter electrode, Ag/AgCl reference electrode, redox standard: decamethylferrocene $E_0^{0/+1} = -0.54$mV (vs. ferrocene $E_0^{0/+1} = 0.00$mV$^{[10]}$)). **Supporting Fig. S94:** Cyclic voltammograms recorded in dichloromethane (T = 293 K, ν = 100 mV/s, electrolyte: [nBu$_4$N][PF$_6$], Pt working electrode, Pt counter electrode, Ag/AgCl reference electrode, redox standard: decamethylferrocene $E_0^{0/+1} = -0.54$mV (vs. ferrocene $E_0^{0/+1} = 0.00$mV$^{[10]}$). **Supporting Fig. S95:** Cyclic voltammograms recorded in dichloromethane (T = 293 K, ν = 100 mV/s, electrolyte: [nBu$_4$N][PF$_6$], Pt working electrode, Pt counter electrode, Ag/AgCl reference electrode, redox standard: decamethylferrocene $E_0^{0/+1} = -0.54$mV (vs. ferrocene $E_0^{0/+1} = 0.00$mV$^{[10]}$)). **Supporting Fig. S96:** Cyclic voltammograms recorded in dichloromethane (T = 293 K, ν = 100 mV/s, electrolyte: [nBu$_4$N][PF$_6$], Pt working electrode, Pt counter electrode, Ag/AgCl reference electrode, redox standard: decamethylferrocene $E_0^{0/+1} = -0.54$mV (vs. ferrocene $E_0^{0/+1} = 0.00$mV$^{[10]}$)). **Supporting Fig. S97:** Cyclic voltammograms recorded in dichloromethane (T = 293 K, ν = 100 mV/s, electrolyte: [nBu$_4$N][PF$_6$], Pt working electrode, Pt counter electrode, Ag/AgCl reference electrode, redox standard: decamethylferrocene $E_0^{0/+1} = -0.54$mV (vs. ferrocene $E_0^{0/+1} = 0.00$mV$^{[10]}$)). **Supporting Fig. S98:** Cyclic voltammograms recorded in dichloromethane (T = 293 K, ν = 100 mV/s, electrolyte: [nBu$_4$N][PF$_6$], Pt working electrode, Pt counter electrode, Ag/AgCl reference electrode, redox standard: decamethylferrocene $E_0^{0/+1} = -0.54$mV (vs. ferrocene $E_0^{0/+1} = 0.00$mV$^{[10]}$)). **Supporting Fig. S99:** Cyclic voltammograms recorded in dichloromethane (T = 293 K, ν = 100 mV/s, electrolyte: [nBu$_4$N][PF$_6$], Pt working electrode, Pt counter electrode, Ag/AgCl reference electrode, redox standard: decamethylferrocene $E_0^{0/+1} = -0.54$mV (vs. ferrocene $E_0^{0/+1} = 0.00$mV$^{[10]}$)). **Supporting Fig. S100:** Cyclic voltammograms recorded in dichloromethane (T = 293 K, ν = 100 mV/s, electrolyte: [nBu$_4$N][PF$_6$], Pt working electrode, Pt counter electrode, Ag/AgCl reference electrode, redox standard: decamethylferrocene $E_0^{0/+1} = -0.54$mV (vs. ferrocene $E_0^{0/+1} = 0.00$mV$^{[10]}$)). **Supporting Fig. S101:** Cyclic voltammograms recorded in dichloromethane (T = 293 K, ν = 100 mV/s, electrolyte: [nBu$_4$N][PF$_6$], Pt working electrode, Pt counter electrode, Ag/AgCl reference electrode, redox standard: decamethylferrocene $E_0^{0/+1} = -0.54$mV (vs. ferrocene $E_0^{0/+1} = 0.00$mV$^{[10]}$)). **Supporting Fig. S102:** Cyclic voltammograms recorded in dichloromethane (T = 293 K, ν = 100 mV/s, electrolyte: [nBu$_4$N][PF$_6$], Pt working electrode, Pt counter electrode, Ag/AgCl reference electrode, redox standard: decamethylferrocene $E_0^{0/+1} = -0.54$mV (vs. ferrocene $E_0^{0/+1} = 0.00$mV$^{[10]}$)). **Supporting Fig. S103:** Cyclic voltammograms recorded in dichloromethane (T = 293 K, ν = 100 mV/s, electrolyte: [nBu$_4$N][PF$_6$], Pt working electrode, Pt counter electrode, Ag/AgCl reference electrode, redox standard: decamethylferrocene $E_0^{0/+1} = -0.54$mV (vs. ferrocene $E_0^{0/+1} = 0.00$mV$^{[10]}$)). **Supporting Fig. S104:** Cyclic voltammograms recorded in dichloromethane (T = 293 K, ν = 100 mV/s, electrolyte: [nBu$_4$N][PF$_6$], Pt working electrode, Pt counter electrode, Ag/AgCl reference electrode, redox standard: decamethylferrocene $E_0^{0/+1} = -0.54$mV (vs. ferrocene $E_0^{0/+1} = 0.00$mV$^{[10]}$)). **Supporting Fig. S105:** Cyclic voltammograms recorded in dichloromethane (T = 293 K, ν = 100 mV/s, electrolyte: [nBu$_4$N][PF$_6$], Pt working electrode, Pt counter electrode, Ag/AgCl reference electrode, redox standard: decamethylferrocene $E_0^{0/+1} = -0.54$mV (vs. ferrocene $E_0^{0/+1} = 0.00$mV$^{[10]}$)). **Supporting Fig. S106:** Cyclic voltammograms recorded in dichloromethane (T = 293 K, ν = 100 mV/s, electrolyte: [nBu$_4$N][PF$_6$], Pt working electrode, Pt counter electrode, Ag/AgCl reference electrode, redox standard: decamethylferrocene $E_0^{0/+1} = -0.54$mV (vs. ferrocene $E_0^{0/+1} = 0.00$mV$^{[10]}$)). **Supporting Fig. S107:** Cyclic voltammograms recorded in dichloromethane (T = 293 K, ν = 100 mV/s, electrolyte: [nBu$_4$N][PF$_6$], Pt working electrode, Pt counter electrode, Ag/AgCl reference electrode, redox standard: decamethylferrocene $E_0^{0/+1} = -0.54$mV (vs. ferrocene $E_0^{0/+1} = 0.00$mV$^{[10]}$)). **Supporting Fig. S108:** Cyclic voltammograms recorded in dichloromethane (T = 293 K, ν = 100 mV/s, electrolyte: [nBu$_4$N][PF$_6$], Pt working electrode, Pt counter electrode, Ag/AgCl reference electrode, redox standard: decamethylferrocene $E_0^{0/+1} = -0.54$mV (vs. ferrocene $E_0^{0/+1} = 0.00$mV$^{[10]}$)). **Supporting Fig. S109:** Cyclic voltammograms recorded in dichloromethane (T = 293 K, ν = 100 mV/s, electrolyte: [nBu$_4$N][PF$_6$], Pt working electrode, Pt counter electrode, Ag/AgCl reference electrode, redox standard: decamethylferrocene $E_0^{0/+1} = -0.54$mV (vs. ferrocene $E_0^{0/+1} = 0.00$mV$^{[10]}$)). **Supporting Fig. S110:** Cyclic voltammograms recorded in dichloromethane (T = 293 K, ν = 100 mV/s, electrolyte:

$[n\mathrm{Bu_4N}][\mathrm{PF_6}]$, Pt working electrode, Pt counter electrode, Ag/AgCl reference electrode, redox standard: decamethylferrocene $E_0^{0/+1} = -0.54\mathrm{mV}$ (vs. ferrocene $E_0^{0/+1} = 0.00\mathrm{mV}$[10]). **Supporting Fig. S111:** Cyclic voltammograms recorded in dichloromethane (T = 293 K, ν = 100 mV/s, electrolyte: $[n\mathrm{Bu_4N}][\mathrm{PF_6}]$, Pt working electrode, Pt counter electrode, Ag/AgCl reference electrode, redox standard: decamethylferrocene $E_0^{0/+1} = -0.54\mathrm{mV}$ (vs. ferrocene $E_0^{0/+1} = 0.00\mathrm{mV}$[10]). **Supporting Fig. S112:** Cyclic voltammograms recorded in dichloromethane (T = 293 K, ν = 100 mV/s, electrolyte: $[n\mathrm{Bu_4N}][\mathrm{PF_6}]$, Pt working electrode, Pt counter electrode, Ag/AgCl reference electrode, redox standard: decamethylferrocene $E_0^{0/+1} = -0.54\mathrm{mV}$ (vs. ferrocene $E_0^{0/+1} = 0.00\mathrm{mV}$[10]). **Supporting Fig. S113:** Cyclic voltammograms recorded in dichloromethane (T = 293 K, ν = 100 mV/s, electrolyte: $[n\mathrm{Bu_4N}][\mathrm{PF_6}]$, Pt working electrode, Pt counter electrode, Ag/AgCl reference electrode, redox standard: decamethylferrocene $E_0^{0/+1} = -0.54\mathrm{mV}$ (vs. ferrocene $E_0^{0/+1} = 0.00\mathrm{mV}$[10]). **Supporting Fig. S114:** Cyclic voltammograms recorded in dichloromethane (T = 293 K, ν = 100 mV/s, electrolyte: $[n\mathrm{Bu_4N}][\mathrm{PF_6}]$, Pt working electrode, Pt counter electrode, Ag/AgCl reference electrode, redox standard: decamethylferrocene $E_0^{0/+1} = -0.54\mathrm{mV}$ (vs. ferrocene $E_0^{0/+1} = 0.00\mathrm{mV}$[10]). **Supporting Fig. S115:** Cyclic voltammograms recorded in dichloromethane (T = 293 K, ν = 100 mV/s, electrolyte: $[n\mathrm{Bu_4N}][\mathrm{PF_6}]$, Pt working electrode, Pt counter electrode, Ag/AgCl reference electrode, redox standard: decamethylferrocene $E_0^{0/+1} = -0.54\mathrm{mV}$ (vs. ferrocene $E_0^{0/+1} = 0.00\mathrm{mV}$[10]). **Supporting Fig. S116:** Cyclic voltammograms recorded in dichloromethane (T = 293 K, ν = 100 mV/s, electrolyte: $[n\mathrm{Bu_4N}][\mathrm{PF_6}]$, Pt working electrode, Pt counter electrode, Ag/AgCl reference electrode, redox standard: decamethylferrocene $E_0^{0/+1} = -0.54\mathrm{mV}$ (vs. ferrocene $E_0^{0/+1} = 0.00\mathrm{mV}$[10]). **Supporting Fig. S117:** Cyclic voltammograms recorded in dichloromethane (T = 293 K, ν = 100 mV/s, electrolyte: $[n\mathrm{Bu_4N}][\mathrm{PF_6}]$, Pt working electrode, Pt counter electrode, Ag/AgCl reference electrode, redox standard: decamethylferrocene $E_0^{0/+1} = -0.54\mathrm{mV}$ (vs. ferrocene $E_0^{0/+1} = 0.00\mathrm{mV}$[10]). **Supporting Fig. S118:** Cyclic voltammograms recorded in dichloromethane (T = 293 K, ν = 100 mV/s, electrolyte: $[n\mathrm{Bu_4N}][\mathrm{PF_6}]$, Pt working electrode, Pt counter electrode, Ag/AgCl reference electrode, redox standard: decamethylferrocene $E_0^{0/+1} = -0.54\mathrm{mV}$ (vs. ferrocene $E_0^{0/+1} = 0.00\mathrm{mV}$[10]). **Supporting Fig. S119:** Cyclic voltammograms recorded in dichloromethane (T = 293 K, ν = 100 mV/s, electrolyte: $[n\mathrm{Bu_4N}][\mathrm{PF_6}]$, Pt working electrode, Pt counter electrode, Ag/AgCl reference electrode, redox standard: decamethylferrocene $E_0^{0/+1} = -0.54\mathrm{mV}$ (vs. ferrocene $E_0^{0/+1} = 0.00\mathrm{mV}$[10]). **Supporting Fig. S120:** Cyclic voltammograms recorded in dichloromethane (T = 293 K, ν = 100 mV/s, electrolyte: $[n\mathrm{Bu_4N}][\mathrm{PF_6}]$, Pt working electrode, Pt counter electrode, Ag/AgCl reference electrode, redox standard: decamethylferrocene $E_0^{0/+1} = -0.54\mathrm{mV}$ (vs. ferrocene $E_0^{0/+1} = 0.00\mathrm{mV}$[10]). **Supporting Fig. S121:** Cyclic voltammograms recorded in dichloromethane (T = 293 K, ν = 100 mV/s, electrolyte: $[n\mathrm{Bu_4N}][\mathrm{PF_6}]$, Pt working electrode, Pt counter electrode, Ag/AgCl reference electrode, redox standard: decamethylferrocene $E_0^{0/+1} = -0.54\mathrm{mV}$ (vs. ferrocene $E_0^{0/+1} = 0.00\mathrm{mV}$[10]). **Supporting Fig. S122:** Cyclic voltammograms recorded in dichloromethane (T = 293 K, ν = 100 mV/s, electrolyte: $[n\mathrm{Bu_4N}][\mathrm{PF_6}]$, Pt working electrode, Pt counter electrode, Ag/AgCl reference electrode, redox standard: decamethylferrocene $E_0^{0/+1} = -0.54\mathrm{mV}$ (vs. ferrocene $E_0^{0/+1} = 0.00\mathrm{mV}$[10]). **Supporting Fig. S123:** Cyclic voltammograms recorded in dichloromethane (T = 293 K, ν = 100 mV/s, electrolyte: $[n\mathrm{Bu_4N}][\mathrm{PF_6}]$, Pt working electrode, Pt counter electrode, Ag/AgCl reference electrode, redox standard: decamethylferrocene $E_0^{0/+1} = -0.54\mathrm{mV}$ (vs. ferrocene $E_0^{0/+1} = 0.00\mathrm{mV}$[10]). **Supporting Fig. S124:** Cyclic voltammograms recorded in dichloromethane (T = 293 K, ν = 100 mV/s, electrolyte: $[n\mathrm{Bu_4N}][\mathrm{PF_6}]$, Pt working electrode, Pt counter electrode, Ag/AgCl reference electrode, redox standard: decamethylferrocene $E_0^{0/+1} = -0.54\mathrm{mV}$ (vs. ferrocene $E_0^{0/+1} = 0.00\mathrm{mV}$[10]). **Supporting Fig. S125:** Cyclic voltammograms recorded in dichloromethane (T = 293 K, ν = 100 mV/s, electrolyte: $[n\mathrm{Bu_4N}][\mathrm{PF_6}]$, Pt working electrode, Pt counter electrode, Ag/AgCl reference electrode, redox standard: decamethylferrocene $E_0^{0/+1} = -0.54\mathrm{mV}$ (vs. ferrocene $E_0^{0/+1} = 0.00\mathrm{mV}$[10]). **Supporting Fig. S126:** Cyclic voltammograms recorded in dichloromethane (T = 293 K, ν = 100 mV/s, electrolyte: $[n\mathrm{Bu_4N}][\mathrm{PF_6}]$, Pt working electrode, Pt counter electrode, Ag/AgCl reference electrode, redox standard: decamethylferrocene $E_0^{0/+1} = -0.54\mathrm{mV}$ (vs. ferrocene $E_0^{0/+1} = 0.00\mathrm{mV}$[10]). **Supporting Fig. S127:** Cyclic voltammograms recorded in dichloromethane (T = 293 K, ν = 100 mV/s, electrolyte: $[n\mathrm{Bu_4N}][\mathrm{PF_6}]$, Pt working electrode, Pt counter electrode, Ag/AgCl reference electrode, redox standard: decamethylferrocene $E_0^{0/+1} = -0.54\mathrm{mV}$ (vs. ferrocene $E_0^{0/+1} = 0.00\mathrm{mV}$[10]). **Supporting Fig. S128:** Cyclic voltammograms recorded in dichloromethane (T = 293 K, ν = 100 mV/s, electrolyte: $[n\mathrm{Bu_4N}][\mathrm{PF_6}]$, Pt working electrode, Pt counter electrode, Ag/AgCl reference electrode, redox standard: decamethylferrocene $E_0^{0/+1} = -0.54\mathrm{mV}$ (vs. ferrocene $E_0^{0/+1} = 0.00\mathrm{mV}$[10]). **Supporting Fig. S129:** Cyclic voltammograms recorded in dichloromethane (T = 293 K, ν = 100 mV/s, electrolyte: $[n\mathrm{Bu_4N}][\mathrm{PF_6}]$, Pt working electrode, Pt counter electrode, Ag/AgCl reference electrode, redox standard: decamethylferrocene $E_0^{0/+1} = -0.54\mathrm{mV}$ (vs. ferrocene $E_0^{0/+1} = 0.00\mathrm{mV}$[10]). **Supporting Fig. S130:** Cyclic voltammograms recorded in dichloromethane (T = 293 K, ν = 100 mV/s, electrolyte: $[n\mathrm{Bu_4N}][\mathrm{PF_6}]$, Pt working electrode, Pt counter electrode, Ag/AgCl reference electrode, redox standard: decamethylferrocene $E_0^{0/+1} = -0.54\mathrm{mV}$ (vs. ferrocene $E_0^{0/+1} = 0.00\mathrm{mV}$[10]). **Supporting Fig. S131:** Cyclic voltammograms recorded in dichloromethane (T = 293 K, ν = 100 mV/s, electrolyte: $[n\mathrm{Bu_4N}][\mathrm{PF_6}]$, Pt working electrode, Pt counter electrode, Ag/AgCl reference electrode, redox standard: decamethylferrocene $E_0^{0/+1} = -0.54\mathrm{mV}$ (vs. ferrocene $E_0^{0/+1} = 0.00\mathrm{mV}$[10]). **Supporting Fig. S132:** Cyclic voltammograms recorded in dichloromethane (T = 293 K, ν = 100 mV/s, electrolyte: $[n\mathrm{Bu_4N}][\mathrm{PF_6}]$, Pt working electrode, Pt counter electrode, Ag/AgCl reference electrode, redox standard: decamethylferrocene $E_0^{0/+1} = -0.54\mathrm{mV}$ (vs. ferrocene $E_0^{0/+1} = 0.00\mathrm{mV}$[10]). **Supporting Fig. S133:** Cyclic voltammograms recorded in dichloromethane (T = 293 K, ν = 100 mV/s, electrolyte: $[n\mathrm{Bu_4N}][\mathrm{PF_6}]$, Pt working electrode, Pt counter electrode, Ag/AgCl reference electrode, redox standard: decamethylferrocene $E_0^{0/+1} = -0.54\mathrm{mV}$ (vs. ferrocene $E_0^{0/+1} = 0.00\mathrm{mV}$[10]). **Supporting Fig. S134:** Cyclic voltammograms recorded in dichloromethane (T = 293 K, ν = 100 mV/s, electrolyte: $[n\mathrm{Bu_4N}][\mathrm{PF_6}]$, Pt working electrode, Pt counter electrode, Ag/AgCl reference electrode, redox standard: decamethylferrocene $E_0^{0/+1} = -0.54\mathrm{mV}$ (vs. ferrocene $E_0^{0/+1} = 0.00\mathrm{mV}$[10]). **Supporting Fig. S135:** Cyclic voltammograms recorded in dichloromethane (T = 293 K, ν = 100 mV/s, electrolyte: $[n\mathrm{Bu_4N}][\mathrm{PF_6}]$, Pt working electrode, Pt counter electrode, Ag/AgCl reference electrode, redox standard: decamethylferrocene $E_0^{0/+1} = -0.54\mathrm{mV}$ (vs. ferrocene $E_0^{0/+1} = 0.00\mathrm{mV}$[10]). **Supporting Fig. S136:** Cyclic voltammograms recorded in dichloromethane (T = 293 K, ν = 100 mV/s, electrolyte: $[n\mathrm{Bu_4N}][\mathrm{PF_6}]$, Pt working electrode, Pt counter electrode, Ag/AgCl reference electrode, redox standard: decamethylferrocene $E_0^{0/+1} = -0.54\mathrm{mV}$ (vs. ferrocene $E_0^{0/+1} = 0.00\mathrm{mV}$[10]). **Supporting Fig. S137:** Cyclic voltammograms recorded in dichloromethane (T = 293 K, ν = 100 mV/s, electrolyte: $[n\mathrm{Bu_4N}][\mathrm{PF_6}]$, Pt working electrode, Pt counter electrode, Ag/AgCl reference electrode, redox standard: decamethylferrocene $E_0^{0/+1} = -0.54\mathrm{mV}$ (vs. ferrocene $E_0^{0/+1} = 0.00\mathrm{mV}$[10]). **Supporting Fig. S138:** Cyclic voltammograms recorded in dichloromethane (T = 293 K, ν = 100 mV/s, electrolyte: $[n\mathrm{Bu_4N}][\mathrm{PF_6}]$, Pt working electrode, Pt counter electrode, Ag/AgCl reference electrode, redox standard: decamethylferrocene $E_0^{0/+1} = -0.54\mathrm{mV}$ (vs. ferrocene $E_0^{0/+1} = 0.00\mathrm{mV}$[10]]). **Supporting Fig. S139:** Absorption and emission spectra of compound **4a** (recorded in dichloromethane, T = 293 K, c_{abs}(**4a**) = 10^{-5} M, c_{em}(**4a**) = 10^{-7} M, $\lambda_{ex} = \lambda_{max,abs}$.). **Supporting Fig. S140:** Absorption and emission spectra of compound **4b** (recorded in dichloromethane, T = 293 K, c_{abs}(**4b**) = 10^{-5} M, c_{em}(**4b**) = 10^{-7} M, $\lambda_{ex} = \lambda_{max,abs}$.). **Supporting Fig. S141:** Absorption and emission spectra of compound **4c** (recorded in dichloromethane, T = 293

K, c_{abs}(**4c**) = 10^{-5} M, c_{em}(**4c**) = 10^{-7} M, $\lambda_{ex} = \lambda_{max,abs}$.). **Supporting Fig. S142:** Absorption and emission spectra of compound **4d** (recorded in dichloromethane, T = 293 K, c_{abs}(**4d**) = 10^{-5} M, c_{em}(**4d**) = 10^{-7} M, $\lambda_{ex} = \lambda_{max,abs}$.). **Supporting Fig. S143:** Absorption and emission spectra of compound **4e** (recorded in dichloromethane, T = 293 K, c_{abs}(**4e**) = 10^{-5} M, c_{em}(**4e**) = 10^{-7} M, $\lambda_{ex} = \lambda_{max,abs}$.). **Supporting Fig. S144:** Absorption and emission spectra of compound **4f** (recorded in dichlorometane, T = 293 K, c_{abs}(**4f**) = 10^{-5} M, c_{em}(**4f**) = 10^{-7} M, $\lambda_{ex} = \lambda_{max,abs}$.). **Supporting Fig. S145:** Absorption and emission spectra of compound **4g** (recorded in dichloromethane, T = 293 K, c_{abs}(**4g**) = 10^{-5} M, c_{em}(**4g**) = 10^{-7} M, $\lambda_{ex} = \lambda_{max,abs}$.). **Supporting Fig. S146:** Absorption and emission spectra of compound **4h** (recorded in dichloromethane, T = 293 K, c_{abs}(**4h**) = 10^{-5} M, c_{em}(**4h**) = 10^{-7} M,.$\lambda_{ex} = \lambda_{max,abs}$). **Supporting Fig. S147:** Absorption and emission spectra of compound 4i (recorded in dichloromethane, T = 293 K, c_{abs}(**4i**) = 10^{-5} M, c_{em}(**4i**) = 10^{-7} M, $\lambda_{ex} = \lambda_{max,abs}$.). **Supporting Fig. S148:** Absorption and emission spectra of compound **4j** (recorded in dichloromethane, T = 293 K, c_{abs}(4j) = 10^{-5} M, c_{em}(**4j**) = 10^{-7} M, $\lambda_{ex} = \lambda_{max,abs}$.). **Supporting Fig. S149:** Absorption and emission spectra of compound **4k** (recorded in dichloromethane, T = 293 K, c_{abs}(**4k**) = 10^{-5} M, c_{em}(4k) = 10^{-7} M, $\lambda_{ex} = \lambda_{max,abs}$.). **Supporting Fig. S150:** Absorption and emission spectra of compound **4l** (recorded in dichloromethane, T = 293 K, c_{abs}(**4l**) = 10^{-5} M, c_{em}(4l) = 10^{-7} M, $\lambda_{ex} = \lambda_{max,abs}$.). **Supporting Fig. S151:** Absorption and emission spectra of compound 4m (recorded in dichloromethane, T = 293 K, c_{abs}(**4m**) = 10^{-5} M, c_{em}(**4m**) = 10^{-7} M, $\lambda_{ex} = \lambda_{max,abs}$.). **Supporting Fig. S152:** Absorption and emission spectra of compound **4n** (recorded in dichloromethane, T = 293 K, c_{abs}(**4n**) = 10^{-5} M, c_{em}(**4n**) = 10^{-7} M, $\lambda_{ex} = \lambda_{max,abs}$.). **Supporting Fig. S153:** Absorption and emission spectra of compound **4o** (recorded in dichloromethane, T = 293 K, c_{abs}(**4o**) = 10^{-5} M, c_{em}(**4o**) = 10^{-7} M, $\lambda_{ex} = \lambda_{max,abs}$.). **Supporting Fig. S154:** Absorption and emission spectra of compound **4p** (recorded in dichloromethane, T = 293 K, c_{abs}(**4p**) = 10^{-5} M, c_{em}(4p) = 10^{-7} M, $\lambda_{ex} = \lambda_{max,abs}$.). **Supporting Fig. S155:** Absorption and emission spectra of compound **4q** (recorded in dichloromethane, T = 293 K, c_{abs}(**4q**) = 10^{-5} M, c_{em}(**4q**) = 10^{-7} M, $\lambda_{ex} = \lambda_{max,abs}$.). **Supporting Fig. S156:** Absorption and emission spectra of compound **4r** (recorded in dichloromethane, T = 293 K, c_{abs}(**4r**) = 10^{-5} M, c_{em}(4r) = 10^{-7} M, $\lambda_{ex} = \lambda_{max,abs}$.). S**upporting Fig. S157:** Absorption and emission spectra of compound 4s (recorded in dichloromethane, T = 293 K, c_{abs}(**4s**) = 10^{-5} M, c_{em}(**4s**) = 10^{-7} M, $\lambda_{ex} = \lambda_{max,abs}$.). **Supporting Fig. S158:** Absorption and emission spectra of compound 4t (recorded in dichloromethane, T = 293 K, c_{abs}(**4t**) = 10^{-5} M, c_{em}(**4t**) = 10^{-7} M, $\lambda_{ex} = \lambda_{max,abs}$.). **Supporting Fig. S159:** Solid-state emission spectra of compound **4a** (recorded at T = 293 K). **Supporting Fig. S160:** Solid-state emission spectra of compound **4b** (recorded at T = 293 K). **Supporting Fig. S161:** Solid-state emission spectra of compound **4c** (recorded at T = 293 K). **Supporting Fig. S162:** Solid-state emission spectra of compound **4d** (recorded at T = 293 K). **Supporting Fig. S163:** Solid-state emission spectra of compound **4e** (recorded at T = 293 K). **Supporting Fig. S164:** Solid-state emission spectra of compound **4f** (recorded at T = 293 K). **Supporting Fig. S165:** Solid-state emission spectra of compound **4f** (recorded at T = 293 K). **Supporting Fig. S166:** Solid-state emission spectra of compound **4h** (recorded at T = 293 K). **Supporting Fig. S167:** Solid-state emission spectra of compound **4i** (recorded at T = 293 K). **Supporting Fig. S168:** Solid-state emission spectra of compound **4j** (recorded at T = 293 K). **Supporting Fig. S169:** Solid-state emission spectra of compound **4k** (recorded at T = 293 K). **Supporting Fig. S170:** Solid-state emission spectra of compound **4l** (recorded at T = 293 K). **Supporting Fig. S171:** Solid-state emission spectra of compound **4m** (recorded at T = 293 K). **Supporting Fig. S172:** Solid-state emission spectra of compound **4n** (recorded at T = 293 K). **Supporting Fig. S173:** Solid-state emission spectra of compound **4o** (recorded at T = 293 K). **Supporting Fig. S174:** Solid-state emission spectra of compound **4o** (recorded at T = 293 K). **Supporting Fig. S175:** Solid-state emission spectra of compound **4q** (recorded at T = 293 K). **Supporting Fig. S176:** Solid-state emission spectra of compound **4r** (recorded at T = 293 K). **Supporting Fig. S177:** Solid-state emission spectra of compound **4s** (recorded at T = 293 K). **Supporting Fig. S178:** Absorption and emission spectra of compound **5a** (recorded in dichloromethane, T = 293 K, c_{abs}(**5a**) = 10^{-5} M, c_{em}(**5a**) = 10^{-7} M, $\lambda_{ex} = \lambda_{max,abs}$.). **Supporting Fig. S179:** Absorption and emission spectra of compound **5b** (recorded in dichloromethane, T = 293 K, c_{abs}(**5b**) = 10^{-5} M, c_{em}(**5b**) = 10^{-7} M, $\lambda_{ex} = \lambda_{max,abs}$.). **Supporting Fig. S180:** Absorption and emission spectra of compound **5c** (recorded in dichloromethane, T = 293 K, c_{abs}(**5c**) = 10^{-5} M, c_{em}(**5c**) = 10^{-7} M, $\lambda_{ex} = \lambda_{max,abs}$.). **Supporting Fig. S181:** Absorption and emission spectra of compound 5d (recorded in dichloromethane, T = 293 K, c_{abs}(**5d**) = 10^{-5} M, c_{em}(**5d**) = 10^{-7} M, $\lambda_{ex} = \lambda_{max,abs}$.). **Supporting Fig. S182:** Absorption and emission spectra of compound **5e** (recorded in dichloromethane, T = 293 K, c_{abs}(**5e**) = 10^{-5} M, c_{em}(**5e**) = 10^{-7} M, $\lambda_{ex} = \lambda_{max,abs}$.). **Supporting Fig. S183:** Absorption and emission spectra of compound 5f (recorded in dichloromethane, T = 293 K, c_{abs}(**5f**) = 10^{-5} M, c_{em}(**5f**) = 10^{-7} M, $\lambda_{ex} = \lambda_{max,abs}$.). **Supporting Fig. S184:** Absorption and emission spectra of compound **5g** (recorded in dichloromethane, T = 293 K, c_{abs}(**5g**) = 10^{-5} M, c_{em}(**5g**) = 10^{-7} M, $\lambda_{ex} = \lambda_{max,abs}$.). **Supporting Fig. S185:** Absorption and emission spectra of compound **5h** (recorded in dichloromethane, T = 293 K, c_{abs}(**5h**) = 10^{-5} M, c_{em}(**5h**) = 10^{-7} M, $\lambda_{ex} = \lambda_{max,abs}$.). **Supporting Fig. S186:** Absorption and emission spectra of compound 5i (recorded in dichloromethane, T = 293 K, c_{abs}(**5i**) = 10^{-5} M, c_{em}(**5i**) = 10^{-7} M, $\lambda_{ex} = \lambda_{max,abs}$.). **Supporting Fig. S187:** Absorption and emission spectra of compound **5j** (recorded in dichloromethane, T = 293 K, c_{abs}(**5j**) = 10^{-5} M, c_{em}(**5j**) = 10^{-7} M, $\lambda_{ex} = \lambda_{max,abs}$.). **Supporting Fig. S188:** Absorption and emission spectra of compound **5k** (recorded in dichloromethane, T = 293 K, c_{abs}(**5k**) = 10^{-5} M, c_{em}(**5k**) = 10^{-7} M, $\lambda_{ex} = \lambda_{max,abs}$.). **Supporting Fig. S189:** Absorption and emission spectra of compound **5l** (recorded in dichloromethane, T = 293 K, c_{abs}(**5l**) = 10^{-5} M, c_{em}(**5l**) = 10^{-7} M, $\lambda_{ex} = \lambda_{max,abs}$.). **Supporting Fig. S190:** Absorption and emission spectra of compound **5m** (recorded in dichloromethane, T = 293 K, c_{abs}(**5m**) = 10_{-5} M, c_{em}(**5m**) = 10^{-7} M, $\lambda_{ex} = \lambda_{max,abs}$.). **Supporting Fig. S191:** Absorption and emission spectra of compound **5n** (recorded in dichloromethane, T = 293 K, c_{abs}(**5n**) = 10^{-5} M, c_{em}(**5n**) = 10^{-7} M, $\lambda_{ex} = \lambda_{max,abs}$.). **Supporting Fig. S192:** Absorption and emission spectra of compound **5o** (recorded in dichloromethane, T = 293 K, c_{abs}(**5o**) = 10^{-5} M, c_{em}(**5o**) = 10^{-7} M, $\lambda_{ex} = \lambda_{max,abs}$.). **Supporting Fig. S193:** Solid-state emission spectra of compound **5a** (recorded at T = 293 K). **Supporting Fig. S194:** Solid-state emission spectra of compound **5b** (recorded at T = 293 K). **Supporting Fig. S195:** Solid-state emission spectra of compound **5c** (recorded at T = 293 K). **Supporting Fig. S196:** Solid-state emission spectra of compound **5d** (recorded at T = 293 K). **Supporting Fig. S197:** Solid-state emission spectra of compound **5e** (recorded at T = 293 K). **Supporting Fig. S198:** Solid-state emission spectra of compound **5f** (recorded at T = 293 K). **Supporting Fig. S199:** Solid-state emission spectra of compound **5g** (recorded at T = 293 K). **Supporting Fig. S200:** Solid-state emission spectra of compound **5h** (recorded at T = 293 K). **Supporting Fig. S201:** Solid-state emission spectra of compound **5i** (recorded at T = 293 K). **Supporting Fig. S202:** Solid-state emission spectra of compound **5j** (recorded at T = 293 K). **Supporting Fig. S203:** Solid-state emission spectra of compound **5k** (recorded at T = 293 K). **Supporting Fig. S204:** Solid-state emission spectra of compound **5l** (recorded at T = 293 K). **Supporting Fig. S205:** Solid-state emission spectra of compound **5m** (recorded at T = 293 K). **Supporting Fig. S206:** Solid-state emission spectra of compound **5n** (recorded at T = 293 K). **Supporting Fig. S207:** Solid-state emission spectra of compound **5o** (recorded at T = 293 K). **Supporting Fig. S208:** Absorption and emission spectra of compound **7a** (recorded in dichloromethane, T = 293 K, c_{abs}(**7a**) = 10^{-5} M, c_{em}(**7a**) = 10^{-7} M, $\lambda_{ex} = \lambda_{max,abs}$.). **Supporting Fig. S209:** Absorption and emission spectra of compound **7b** (recorded in dichloromethane, T = 293 K, c_{abs}(**7b**) = 10^{-5} M, c_{em}(**7b**) = 10^{-7} M, $\lambda_{ex} = \lambda_{max,abs}$.). **Supporting Fig. S210:** Absorption and emission spectra of compound **7c** (recorded in dichloromethane, T = 293 K, c_{abs}(**7c**) = 10^{-5} M, c_{em}(**7c**) = 10^{-7} M, $\lambda_{ex} = \lambda_{max,abs}$.). **Supporting Fig. S211:** Absorption and emission spectra of compound **7d** (recorded in dichloromethane, T = 293 K, c_{abs}(**7d**) = 10^{-5} M, c_{em}(**7d**) = 10^{-7} M, $\lambda_{ex} = \lambda_{max,abs}$.). **Supporting Fig. S212:** Solid-state emission spectra of compound **7a** (recorded at T = 298 K). **Supporting Fig. S213:** Solid-state emission spectra of compound **7b** (recorded at T = 293 K). **Supporting Fig. S214:** Solid-state emission spectra of compound **7c** (recorded at T = 293 K). **Supporting Fig. S215:** Solid-state emission spectra of compound **7d** (recorded at T = 293 K). **Supporting Fig. S216:** Absorption and emission spectra of compound **8a** (recorded in dichloromethane, T = 293 K, c_{abs}(**8a**) = 10^{-5} M, c_{em}(**8a**) = 10^{-7} M, $\lambda_{ex} = \lambda_{max,abs}$.). **Supporting Fig. S217:** Absorption and emission spectra of compound **8b** (recorded in dichloromethane, T = 293

K, c_{abs}(**8b**) = 10^{-5} M, c_{em}(**8b**) = 10^{-7} M, $\lambda_{ex} = \lambda_{max,abs.}$). **Supporting Fig. S218:** Absorption and emission spectra of compound **8c** (recorded in dichloromethane, T = 293 K, c_{abs}(**8c**) = 10^{-5} M, c_{em}(**8c**) = 10^{-7} M, $\lambda_{ex} = \lambda_{max,abs.}$). **Supporting Fig. S219:** Absorption and emission spectra of compound 8d (recorded in dichloromethane, T = 293 K, c_{abs}(**8d**) = 10^{-5} M, c_{em}(**8d**) = 10^{-7} M, $\lambda_{ex} = \lambda_{max,abs.}$). **Supporting Fig. S220:** Absorption and emission spectra of compound **8e** (recorded in dichloromethane, T = 293 K, c_{abs}(**8e**) = 10^{-5} M, c_{em}(**8e**) = 10^{-7} M, $\lambda_{ex} = \lambda_{max,abs.}$). **Supporting Fig. S221:** Absorption and emission spectra of compound **8f** (recorded in dichloromethane, T = 293 K, c_{abs}(**8f**) = 10^{-5} M, c_{em}(**8f**) = 10^{-7} M, $\lambda_{ex} = \lambda_{max,abs.}$). **Supporting Fig. S222:** Solid-state emission spectra of compound **8a** (recorded at T = 293 K). **Supporting Fig. S223:** Solid-state emission spectra of compound **8b** (recorded at T = 293 K). **Supporting Fig. S224:** Solid-state emission spectra of compound **8c** (recorded at T = 293 K). **Supporting Fig. S225:** Solid-state emission spectra of compound **8d** (recorded at T = 293 K). **Supporting Fig. S226:** Solid-state emission spectra of compound **8e** (recorded at T = 293 K). **Supporting Fig. S227:** Solid-state emission spectra of compound **8f** (recorded at T = 293 K). **Supporting Fig. S228:** Comparison of the calculated (Gaussian 16, PBE1PBE/6 31+G**, PCM CH_2Cl_2) and experimentally determined (recorded in CH_2Cl_2, T = 293 K, c = 10^{-5} m) UV/Vis spectrum of *sym-m*-bTAA **4k** with the calculated transitions as bars (left). Calculated molecular orbitals (Gaussian 16, PBE1PBE/6 31+G**, PCM CH_2Cl_2, isosurface value at 0.025 a.u.) of **4k** for the HOMO → LUMO transition and the three dominant energy transitions (right). **Supporting Fig. S229:** Correlation of the energy difference ΔE between the HOMO energy E_{HOMO} and the LUMO energy E_{LUMO} with the substituent parameter of *sym-m*-bTAA **4h**-l with a phenyl substituent in the biaryl moiety (R^1 = H (constant)) (Gaussian 16, PBE1PBE/6-31+G**, PCM CH_2Cl_2, $\Delta E(E_{HOMO}\text{-}E_{LUMO})$ = 0.321 eV, $\sigma_p^+ + 4.404$eV, r^2 = 0.998). **Supporting Fig. S230:** Correlation of calculated emission maxima with the substituent parameter $\sigma_p^{+[11]}$ of *sym-m*-bTAA **4h-l** with a phenyl substituent in the biaryl moiety (R^1 = H (constant)) (Gaussian 16, PBE1PBE/6-31+G**, PCM CH_2Cl_2, $\tilde{\nu}_{Em,calc} = 4270\text{cm}^{-1}$, $\sigma_p^+ + 24374\text{cm}^{-1}$, r^2 = 0.999). **Supporting Fig. S231:** Correlation of calculated Stokes shift with the substituent parameter $\sigma_p^{+[11]}$ of *sym-m*-bTAA **4h-l** with a phenyl substituent in the biaryl moiety (R^1 = H (constant)) (Gaussian 16, PBE1PBE/6-31+G**, PCM CH_2Cl_2, $\Delta\tilde{\nu}_{s,calc} = 2259\text{cm}^{-1}$, $\sigma_p^+ + 4381\text{cm}^{-1}$, $r^2 = 0.985$). **Supporting Fig. S232:** Correlation of the energy difference ΔE between the HOMO energy E_{HOMO} and the LUMO energy E_{LUMO} with the substituent parameter of sym-m-bTAA 4b, **4f**, **4k**, **4n**, **4p,** and **4r** with phenyl substituents on the central nitrogen atom (R^2 = H (constant)) (Gaussian 16, PBE1PBE/6-31+G**, PCM CH2Cl2, $\Delta E(E_{HOMO}\text{-}E_{LUMO})$ = −0.600 eV σ_p^- + 4.412eV, r^2 = 0.967). **Supporting Fig. S233:** Correlation of calculated emission maxima with the substituent parameter $\sigma_p^{-[11]}$ of *sym-m*-bTAA **4b**, **4f**, **4k**, **4n**, **4p,** and **4r** with phenyl substituents on the central nitrogen atom (R^2 = H (constant)) (Gaussian 16, PBE1PBE/6-31+G**, PCM CH_2Cl_2, $\tilde{\nu}_{Em,calc} = -4376\text{cm}^{-1}$ σ_p^- + 24734cm^{-1}, r^2 = 0.955). **Supporting Fig. S234:** Comparison of the calculated (Gaussian 16, PBE1PBE/6 31+G**, PCM CH_2Cl_2) and experimentally determined (recorded in CH_2Cl_2, T = 293 K, $c = 10^{-5}$ m) UV/Vis spectrum of *sym-o*-bTAA **5g** with the calculated transitions as bars (left). Calculated molecular orbitals (Gaussian 16, PBE1PBE/6 31+G**, PCM CH_2Cl_2, isosurface value at 0.025 a.u.) of **5g** for the HOMO → LUMO transition and the three dominant energy transitions (right). **Supporting Fig. S235:** Correlation of the energy difference ΔE between the HOMO energy E_{HOMO} and the LUMO energy E_{LUMO} with the substituent parameter of *sym-o*-bTAA **5e-h** with a phenyl substituent in the biaryl moiety (R^1= H (constant)) (Gaussian 16, PBE1PBE/6-31+G**, PCM CH_2Cl_2, $\Delta(E_{HOMO}\text{-}E_{LUMO})$ = 0.407 eV, r^2 = 0.989). **Supporting Fig. S236:** Correlation of calculated emission maxima with the substituent parameter $\sigma_p^{+[11]}$ of *sym-o*-bTAA **5e-h** with a phenyl substituent in the biaryl moiety (R^1 = H (constant)) (Gaussian 16, PBE1PBE/6-31+G**, PCM CH_2Cl_2, $\tilde{\nu}_{Em,calc} = 3946\text{cm}^{-1} \cdot \sigma_p^+ + 24097\text{cm}^{-1}$, $\cdot r^2$ = 0.996). **Supporting Fig. S237:** Correlation of calculated Stokes shift with the substituent parameter $\sigma_p^{+[11]}$ of *sym-o*-bTAA **5e-h** with a phenyl substituent in the biaryl moiety (R^1 = H (constant)) (Gaussian 16, PBE1PBE/6-31+G**, PCM CH_2Cl_2, $\Delta\tilde{\nu}_{s,calc} = -1065\text{cm}^{-1} \cdot \sigma_p^+ + 4920\text{cm}^{-1}$, r^2 = 0.998). **Supporting Fig. S238:** Correlation of the energy difference ΔE between the HOMO energy E_{HOMO} and the LUMO energy E_{LUMO} with the substituent parameter $\sigma_p^{+[11]}$ of *sym-o*-bTAA **5c**, **5g**, **5j**, **5l,** and **5n** with phenyl substituents on the central nitrogen atom (R^2 = H (constant)) (Gaussian 16, PBE1PBE/6-31+G**, PCM CH_2Cl_2, $\Delta E(E_{HOMO}\text{-}E_{LUMO})$ = 0.574 eV σ_p^- + 4.505eV, r^2 = 0.954). **Supporting Fig. S239:** Correlation of calculated emission maxima with the substituent parameter $\sigma_p^{-[11]}$ of *sym-o*-bTAA **5c**, **5g**, **5j**, **5l,** and **5n** with phenyl substituents on the central nitrogen atom (R^2 = H (constant)) (Gaussian 16, PBE1PBE/6-31+G**, PCM CH_2Cl_2, $\tilde{\nu}_{Em,calc} - 3177\text{cm}^{-1} \cdot \sigma_p^- + 24063\text{cm}^{-1}$, r^2 = 0.995). **Supporting Fig. S240:** Time-dependent emission intensity of sym-m-bTAA **4q** and *sym-o*-bTAA **5m** at a water content of 80% (T = 293 K, $c = 10^{-7}$ M). **Supporting Table S1:** Experimental details for the synthesis of *sym-m*-bTAA **4**. **Supporting Table S2:** Chemical shifts of the relevant compounds in the ^{19}F NMR spectrum. **Supporting Table S3:** Experimental details on the optimization of the amount of 1-bromo-4-fluorobenzene **3e** used for the preparation of *sym-o*-bTAA **5d** via MCR. **Supporting Table S4:** Experimental details for the synthesis of *sym-o*-bTAA **5**. **Supporting Table S5:** Experimental details for the synthesis of *sym-m*/*o*-Br-TAAs **6**. **Supporting Table S6:** Experimental details for the synthesis of *sym-m*/*o*-bTAA **4** and **5**. **Supporting Table S7:** Experimental details for the synthesis of *unsym-m*-bTAA 7. **Supporting Table S8:** Experimental details for the synthesis of *unsym-o*-bTAA 8. **Supporting Table S9:** Bond lengths and angles from the crystal structures of *sym-p*-bTAA A and *sym-o*-bTAA 5. **Supporting Table S10:** Crystal structure data for **5c**. **Supporting Table S11:** Crystal structure data for **5g**. **Supporting Table S12:** Crystal structure data for **5m**. **Supporting Table S13:** Crystal structure data for **5n**. **Supporting Table S14:** TD-DFT calculations for the UV/Vis absorption and emission maxima of *sym-m*-bTAA **4b**, **4f**, **4h**-l, **4n**, **4p,** and **4r** (Gaussian 16, PBE1PBE/6-31+G**, PCM CH_2Cl_2). **Supporting Table S15:** TD-DFT calculations for the UV/Vis absorption and emission maxima of *sym-o*-bTAA **5c**, **5e-h**, **5j**, **5l,** and **5n** (Gaussian 16, PBE1PBE/6-31+G**, PCM CH_2Cl_2). **Supporting Table S16:** Tabular overview of the utilized parameters.[11] **Supporting Table S17:** Tabular overview of the utilized values of *sym-m*-bTAA **4q**. **Supporting Table S18:** Tabular overview of the utilized values of sym-o-bTAA **8m**.